Stellar Evolution at the Crossroads: Resolving the Nature of RV Tauri Variable Systems Using Unprecedented Observations From the Kepler and XMM–Newton Space Telescopes

By

Laura Daniela Vega

Dissertation

Submitted to the Faculty of the

Graduate School of Vanderbilt University

in partial fulfillment of the requirements

for the degree of

DOCTOR OF PHILOSOPHY

in

Astrophysics

March 31, 2021

Nashville, Tennessee

Approved:

Keivan G. Stassun, Ph.D.

Andreas A. Berlind, Ph.D.

Patricia T. Boyd, Ph.D.

J. Kelly Holley-Bockelmann, Ph.D.

Rodolfo Montez Jr., Ph.D.

Eric M. Schlegel, Ph.D.

DEDICATION

I dedicate this dissertation to all those who have inspired, encouraged, mentored, cared, and supported me on this journey to become an astrophysicist.

ACKNOWLEDGMENTS

This PhD could not have been possible on my own. I would like to take this moment to express my sincere thanks to all my family and friends who have cheered me on from the start. And to all the gentle people who have crossed my path, who I have either learned from or who have simply been kind to me at any point in this journey, thank you. Gabriel, thank you for your encouraging words and the countless moments you boosted my self-esteem when I did not believe in myself... Thank you for believing in me. Un agradecimiento especial a mama, daddy, Adriana, y Joel por su amor incondicional. Daddy (my Luna) and Mama (my Vega): gracias por llevarnos a México a visitar familia cada verano desde que éramos pequeños. Admirando el cielo repleto de estrellas durante nuestros viajes de noche en carretera, en el bello desierto montaoso Mexicano, fue una de mis inspiraciones para querer estudiar el universo. ¡Lo logré, mama! Jesse, thank you for your love, support, and caring. And for all the little but meaningful things you do for us, they have kept me going, especially when finishing this dissertation, they do not go unnoticed. And for our little kitty cat, Logan, who makes me smile just by being a cat. To my advisor Keivan and my research mentor Rudy: my sincerest thanks for giving me the opportunity of working with you at Vanderbilt, and at the Center for Astrophysics. I am very grateful for your constant support, motivation, guidance, time, and patience, as well as the sincere words of advice you have given me during some difficult moments in my life. I would also like to thank the rest of the members of my dissertation committee, Eric Schlegel, Padi Boyd, Kelly Holley-Bockelmann, and Andreas Berlind: thank you for your time, expertise, advice, and kindness. I would like to acknowledge Vanderbilt's Psychological & Counseling Center and Center for Student Wellbeing, especially Samantha York: my academic coach, meditation guide, and Writer's Accountability Group mentor. I would not have made it this far without the support and resources they provided. I would like to thank the Fisk-Vanderbilt Master's-to-PhD Bridge Program family for all of the support they have given me. I am grateful to my NASA OSTEM family and to the SREB Institute for Teaching and Mentoring. I would like to acknowledge the wonderful work of the NASA's Goddard Space Flight Center's

Astrophysics Science Division Communications Team in the production of a NASA news feature for our research. I am very grateful this dissertation work was financially supported by the NASA OSTEM MUREP Harriett G. Jenkins Predoctoral Fellowship, Grant Nos. NNX15AU33H and 80NSSC19K1292; by the partial federal support from the Latino Initiatives Pool, administered by the Smithsonian Latino Center; and by the partial support from NSF PAARE grant AST-1358862.

This research has made use of XMM–*Newton*, an ESA Science Mission with instruments and contributions directly funded by ESA Member States and the USA (NASA).

This research has made use of The Submillimeter Array, a joint project between the Smithsonian Astrophysical Observatory and the Academia Sinica Institute of Astronomy and Astrophysics and is funded by the Smithsonian Institution and the Academia Sinica.

We acknowledge with thanks the variable star observations from the AAVSO International Database contributed by observers worldwide and used in this research.

This research has made use of the DASCH project at Harvard, which is grateful for partial support from NSF grants AST-0407380, AST-0909073, and AST-1313370.

This research has made use of the SIMBAD database, operated at CDS, Strasbourg, France, and of the VizieR catalog access tool, CDS, Strasbourg, France (DOI: 10.26093/cds/vizier). The original description of the VizieR service was published in 2000 (Ochsenbein et al., 2000).

This work includes data collected by the Kepler mission. Funding for the Kepler mission is provided by the NASA Science Mission directorate. The data was obtained from the Mikulski Archive for Space Telescopes (MAST). STScI is operated by the Association of Universities for Research in Astronomy, Inc., under NASA contract NAS5-26555. Support for MAST for non-HST data is provided by the NASA Office of Space Science via grant NNX09AF08G and by other grants and contracts.

This work makes use of data products from the Two Micron All Sky Survey, which is a joint project of the University of Massachusetts and the Infrared Processing and Analysis Center/California Institute of Technology, funded by the National Aeronautics and Space Administration and the National Science Foundation.

TABLE OF CONTENTS

Page

LIST OF TABLES

LIST OF FIGURES

Chapter 1

Introduction

1.1 RV Tauri Variables

The discovery of RV Tauri stars was more than 100 years ago, yet their physical processes and evolutionary origin still remain poorly understood. These pulsating stars were recognized as a distinct class of variables in 1905[1] after the discovery of their prototype-star, RV Tauri, (Ceraski, 1905). RV Tauri stars are primarily identified by their signature pulsation pattern in their light curves that show a sinusoidal wave with alternating deep and shallow minima in brightness with periods ranging between 20–150 days (Figure 1.1).

RV Tauri stars extend the brightest part of the Type II Cepheid period-luminosity relationship (Figure 1.2), however, the pulsations of RV Tauri stars are not strictly regular and they show more cycle-to-cycle scatter, than those of the other Type II Cepheid subclasses (e.g., BL Hercules and W Virginis stars; Catelan & Smith, 2015). RV Tauri stars reside near the brightest part of the instability strip[2] on the Hertzsprung–Russell (luminosity–versus–temperature) diagram, where high-mass and low-mass single-star evolutionary tracks meet (Cox, 1974, see Figure 1.3). Studies favor the lower–mass stellar origin for RV Tauri stars (e.g., Willson & Templeton, 2009), and are defined as a subclass of post-asymptotic giant branch (AGB) stars from low-to-intermediate-mass stars between 0.8–8 $M_{\odot}$ (van Winckel, 2018). However they span a diverse group of stars, for example, recent studies have shown that RV Tauri stars can also be post-red giant branch (RGB) stars (e.g., Kamath, 2015), which have similar stellar parameters as their post-AGB counterparts but appear at lower luminosities. The post-AGB identification (also dubbed as 'pre-planetary nebula'), of RV Tauri stars is owing to their high luminosity, mass-loss history, and large infrared excess in their spectral energy distribution due to circumstellar dust (Jura, 1986), see Figure 1.4.

[1] For a nice highlight of RV Tau, see https://www.aavso.org/vsots_rvtau

[2] The instability strip is a narrow region on the Hertzsprung–Russell diagram largely occupied by several classes of pulsating variable stars.

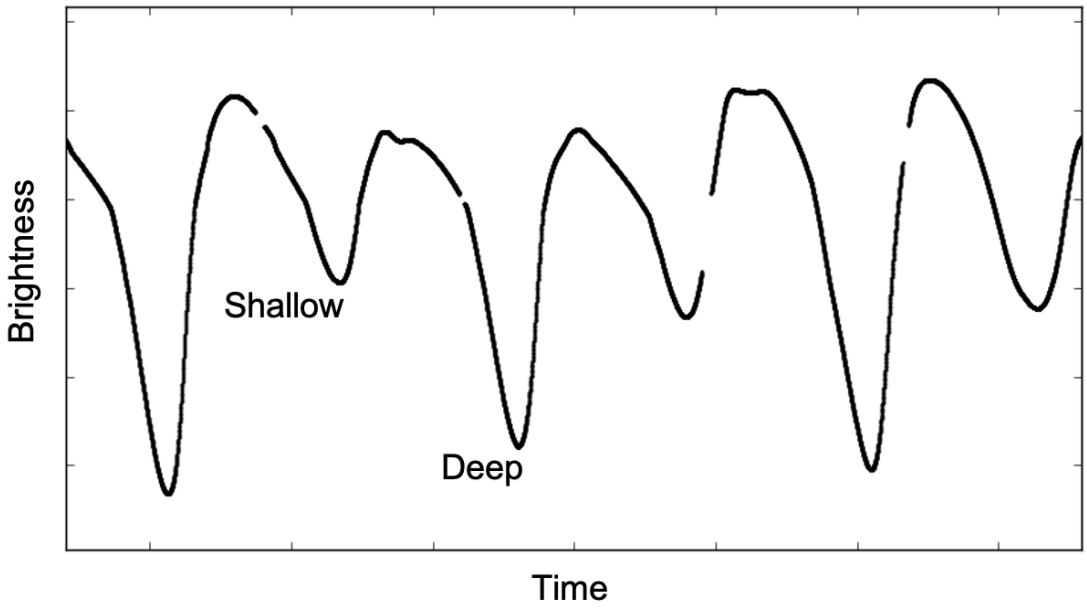

Figure 1.1: A segment of DF Cygni's *Kepler* light curve, an RV Tauri-type variable star, showing the characteristic pulsation pattern of alternating deep and shallow minima in brightness over time.

The internal structure of a star at the AGB phase consists of a degenerate carbon and oxygen core with hydrogen- and helium-burning shells surrounding it, followed by a highly–extended envelope. During the AGB phase rich nucleosynthesis occurs where carbon, nitrogen, oxygen, and slow neutron capture (s-process)[3] elements, beyond iron, are produced (Höfner & Olofsson, 2018). The transition between the AGB and post-AGB is not clearly defined but the late AGB phase is driven by large-scale pulsations, where the star at the post-AGB phase (10^3–10^5 yr, depending on the star's initial mass), undergoes an increase of mass-loss ranging between 10^{-7} and 10^{-4} $M_\odot$ yr^{-1} (van Winckel, 2003).

The stellar giant's outer-most atmosphere continues to expand out by the X-ray–emitting (e.g., Montez et al., 2015) hot ($>$ 30 kK) and luminous core (10^3–10^4 $L_\odot$), which ionizes the loosely-bound stellar material. Shells of slowly ejected material eventually form a beautiful planetary nebula (see Figure 1.5). However the majority ($\sim$ 80%) of planetary nebulae do not seem to follow

[3] The s-process is a series of nuclear reactions where a seed nucleus undergoes neutron capture to form heavier elements.

a spherically symmetric release of its outer layers, and reveal a variety of complex morphologies (De Marco, 2009). The mechanisms that produce the different planetary nebula shapes and features are not well understood, but binarity, stellar rotation, snow-plowing mechanisms, and magnetic fields affecting the strong stellar winds seem to play a big role (e.g., Balick & Frank, 2002; Sahai et al., 2011).

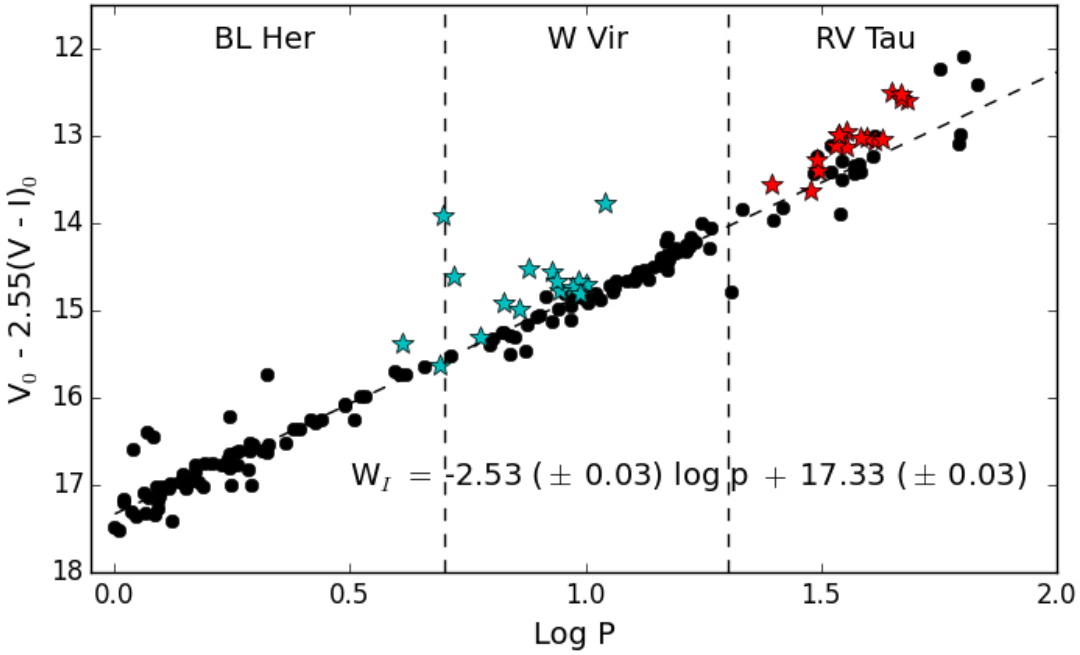

Figure 1.2: The relationship between brightness and pulsation (i.e., the Leavitt Law) for Type II Cepheid variables in the Large Magellanic Cloud. The cyan and red symbols are "peculiar" W Vir stars and highly-reddened RV Tauri stars, respectively, and were not used in the linear regression model show in this plot. Figure take from Manick et al. (2017).

Various studies (e.g., van Winckel et al., 1999; Maas et al., 2002; de Ruyter et al., 2005; Gezer et al., 2015; Manick et al., 2017) have argued that the RV Tauri subclass of post-AGB stars can generally be understood if they possess binary companions within the presence of a stable circumbinary disk surrounding both stars. van Winckel et al. (1999) compared various observed characteristics of RV Tauri stars with other post-AGBs in known binary systems and found that a high fraction of RV Tauri stars were similar to their binary post-AGB counterparts.

Some RV Tauri variables also exhibit a longer-term ($\sim 10^2$–10^3 days) variation in mean brightness and are know as the RVb-subclass. It was debated if this variation was due to changes from

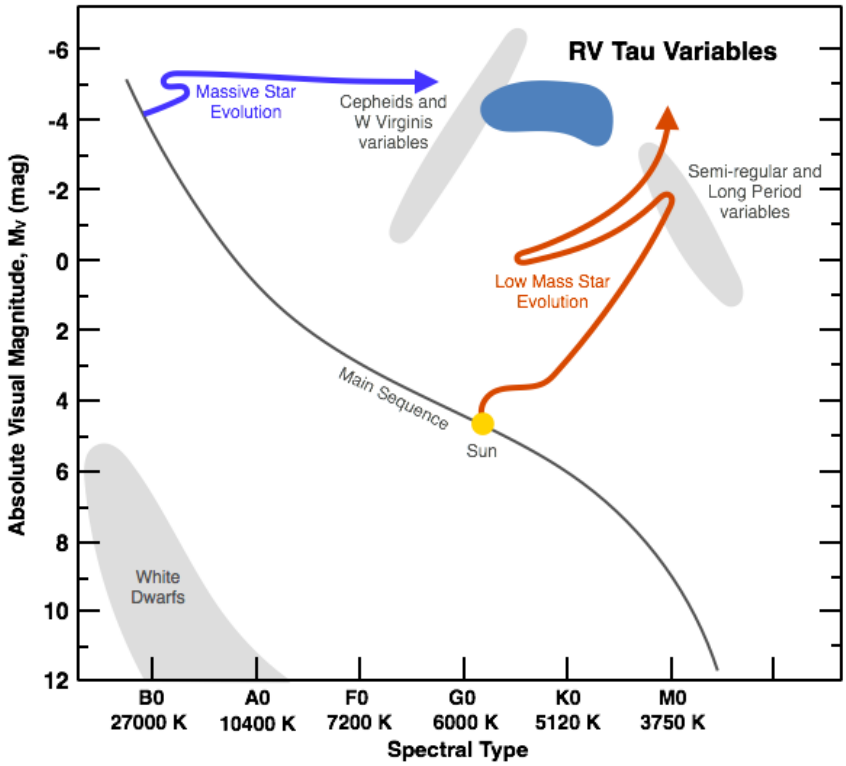

Figure 1.3: RV Tauri stars reside in a part of the HR diagram where stellar evolutionary tracks of high mass and low mass stars meet, they were thought to evolve from either massive or low-mass stars. Recent studies favor a low-mass stellar origin. Figure adapted from Cox (1974).

the pulsating star itself or if it was an extrinsic variable extinction by dust that surrounds either or both stars (e.g., Percy, 1993). However recent discoveries favor the disk-obscuration model (e.g., Kiss & Bódi, 2017). The structure of the circumbinary disks around these post-AGB binaries have therefore been found to be important in understanding the evolution of the systems themselves. Looking for tracers for the evolution and lifetime of the circumbinary disk may give estimates to the binary-evolution process in RV Tauri systems, as they can evolve the eccentricity of the binary.

Most recently, studies have also shown on-going outflows, likely emerging from the circum-companion environment of the companion star in post-AGB binaries caused by accretion due to interactions within the system (e.g. Gorlova et al., 2012; Bollen et al., 2019; Oomen et al., 2019). Though it is accepted that binarity affect the evolution of low-to-intermediate mass stars at late stages of evolution, there is still missing physics that needs to be explored.

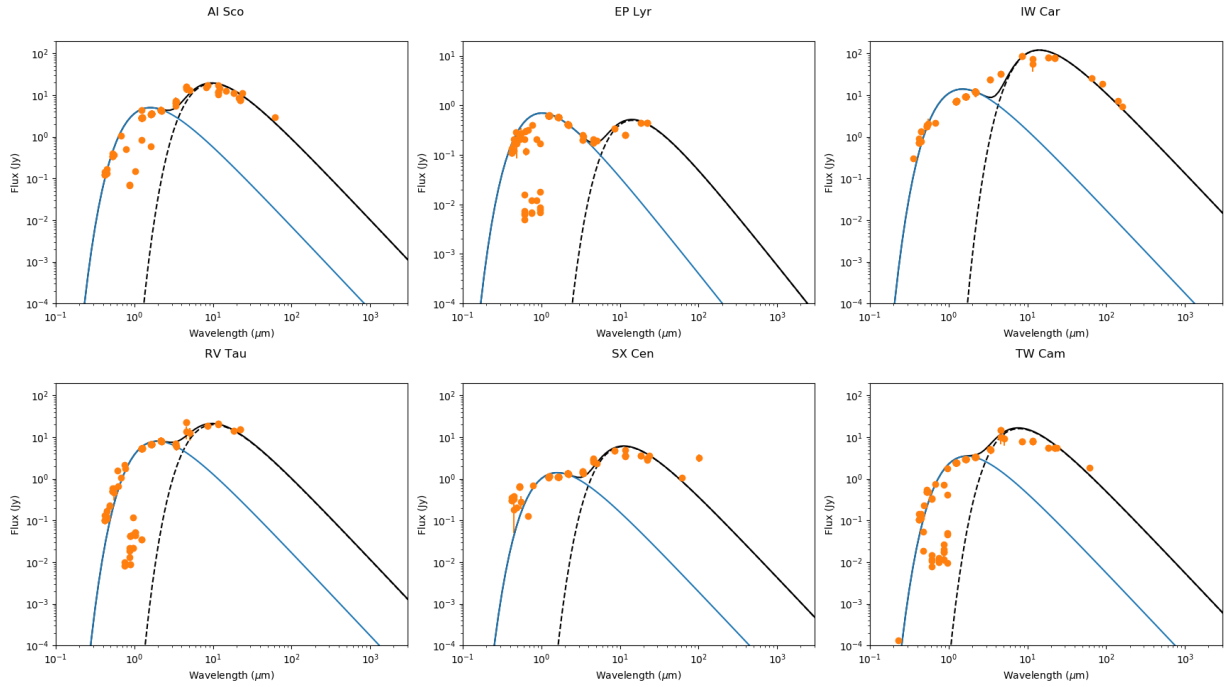

Figure 1.4: Spectral energy distributions of six bright RV Tauri stars showing an excess of infrared light starting at $\sim$2 μm. All except for EP Lyr (top second panel) display the photometric RVb phenomenon in their light curves. The raw broadband photometric data in these figures were downloaded from vizieR and have not been corrected for foreground extinction. The solid blue and dashed black lines are scaled blackbody components depicting the stellar atmosphere emission and the infrared excess (indicative of dust in the system), respectively. These blackbody models are not fitted to the data.

1.2 Dissertation Outline

In order to better understand the characteristics exhibited by RV Tauri variables, the environment in which they form, and to explain their place in stellar evolution, this dissertation focuses on using observations obtained by the NASA-led *Kepler* and ESA-led XXM–*Newton* space missions, as well as photometric observations that date back to the late 1880s. One of open questions that this work has helped to confirm is the cause for the photometric RVb variability. In Chapter 2 we provide an observational analysis of the RVb variable DF Cygni, the only RV Tauri system in *Kepler*'s original field-of-view. Using the highly-resolved *Kepler* light curve, we establish that DF Cyg's slow RVb phenomenon is due to an orbital modulation where an opaque body periodically obscures the pulsating star by 90% every $\sim$ 800 days. This opaque screen is the circumbinary

disk surrounding the binary system.

In Chapter 3 we discuss the X-ray emission for the RVb binary, U Monocerotis (U Mon), which is the first RV Tauri system to be detected in X rays. U Mon is also the first RV Tauri system with a clear discovery of weak magnetic fields at the stellar surface (Sabin et al., 2015). From U Mon's $\sim$ 130 year light curve, we find longer-term secular variations on the RVb phenomenon that are in the order of decades and suspect is caused by the circumbinary disk. Our work on U Mon spans the largest range of wavelengths (X-ray to millimeter) and the longest range of time. We propose that the X-ray emission may be coming from the stellar companion, perhaps a circumcompanion accretion disk surrounding it. Such accretion disks have also been observed in other post-AGB binary stars (e.g., Bollen et al., 2017) and are related to Hα variations due to orbital motion. However, more observations are needed to confirm if there are any correlations between Hα variations, X-ray emission, and magnetic fields in U Mon and in other systems. Finally, in Chapter 4 we discuss future work. The newly detection of X-rays in an RV Tauri system, has now opened up new possibilities to consider, and can enable constraints on the stellar evolution for late-stage binary systems. Furthermore, historic DASCH data will help to understand the long-term behavior of circumbinary disks around these stars. With the radial velocity monitoring, which began in 2009 (Raskin et al., 2011), long-period RV Tauri systems are starting to accumulate more data, this with the combination of monitoring them at other wavelengths, will further shed much needed light onto these mysterious evolved systems.

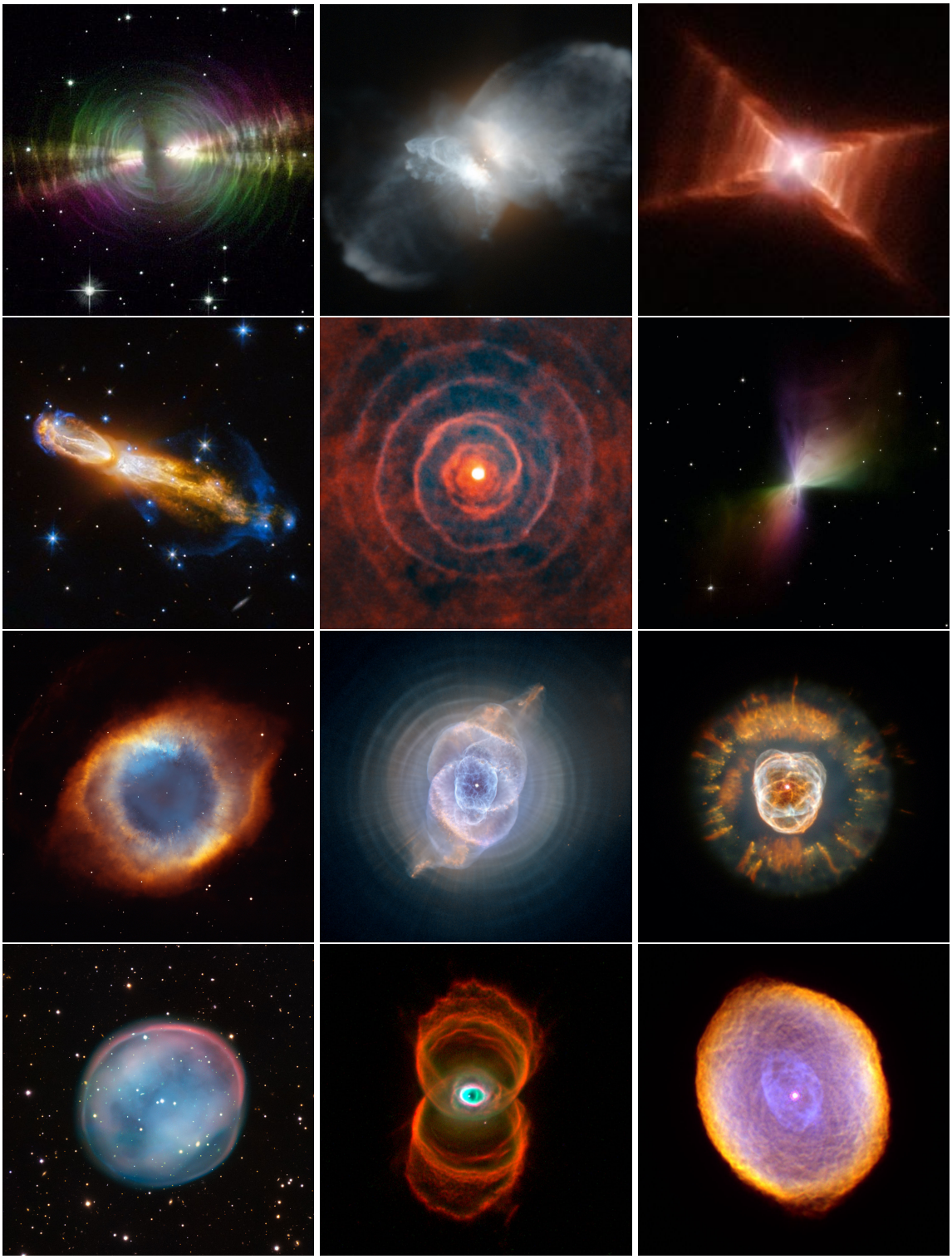

Figure 1.5: False color images of preplanetary nebulae (first two rows) and planetary nebulae (bottom two rows). Top row (left to right): Egg Nebula (V1610 Cyg), Frosty Leo Nebula (IRAS 09371+1212), Red Rectangle (HD 44179). Second row (left to right): Calabash Nebula (OH 231.8+4.2), LL Pegasi (AFGL 3068), Boomerang Nebula. Third row (left to right): Helix Nebula (NGC 7293), Cat's Eye Nebula (NGC 6543), Lion Nebula (NGC 2392). Last row (left to right): Southern Owl (ESO 378-1), Hourglass Nebula (MyCn18), Spirograph Nebula (IC 418). Image Credit: NASA and The Hubble Heritage Team, ESA, and ESO.

Chapter 2

Evidence for Binarity and Possible Disk Obscuration in *Kepler* Observations of the Pulsating RV Tau Variable DF Cygni

The following work was originally published in The Astrophysical Journal (Vega et al., 2017) and is reprinted below in its entirety.

Laura D. Vega[1,2], Keivan G. Stassun[1,2], Rodolfo Montez Jr.[3], Patricia T. Boyd[4], Garrett Somers[1,5]

[1]Department of Astrophysics, Vanderbilt University, Nashville, TN, USA

[2]Department of Physics, Fisk University, Nashville, TN, USA

[3]Harvard-Smithsonian Center for Astrophysics, Cambridge, MA, USA

[4]NASA Goddard Space Flight Center, Greenbelt, MD, USA

[5]VIDA Postdoctoral Fellow

2.1 Original Abstract

The *Kepler* light curve of DF Cyg is unparalleled in precision and cadence for any RV Tau star to date spanning a baseline of $\sim$4 years and clearly displaying the signature pulsating behavior of alternating deep and shallow minima as well as the long-term trend indicative of an RVb-type variable. We measure DF Cyg's formal period (the time interval between two successive deep minima) to be 49.84 ± 0.02 days. The trend in the arrival times emulates that of the long-term period. There appear to be precisely 16 deep+shallow minima cycles in one long-term cycle, suggesting a long-term cycle period of $\approx 795 \pm 5$ days. We argue that binarity may naturally explain the long-term periodicity in DF Cyg. The spectral energy distribution of DF Cyg features an infrared excess indicative of a disk possibly linked to a binary companion. From a recent *Gaia* parallax measurement for DF Cyg, we calculated that it has a distance of 990 ± 372 pc and a physical radius of $R_\star = 10.3 \pm 3.8$ $R_\odot$. From kinematics and geometric arguments, we argue that the most likely interpretation for the decrease in flux from the long-period maximum to the long-period minimum, as well as the reduction of the short-term pulsation amplitude, is caused by an occulting body such as a disk surrounding DF Cyg and its binary companion.

2.2 Introduction

RV Tau variable stars, named after their prototype RV Tauri, are luminous large-amplitude pulsating supergiants (General Catalog of Variable Stars (GCVS); Samus et al., 2009) located at the brightest part of the population Type II Cepheid instability strip in the Hertzsprung–Russell diagram (Wallerstein, 2002). The colors of RV Tau stars are in phase with their variation in brightness, displaying spectral types between F and G at maximum light and K to M at minimum light (Samus et al., 2009). The large luminosities and large IR excess due to circumstellar dust exhibited by RV Tau variables led to their classification as post-asymptotic giant branch (post-AGB) objects, suggesting they can be planetary nebula progenitors (Jura, 1986).

The main characteristic of RV Tau variables is a double wave of alternating deep and shallow minima in their light curve. The combination of deep and shallow minima has a "formal" period (the time interval between two successive deep minima) that ranges between 30 and 150 days (Samus et al., 2009). This short-term feature of repeating deep and shallow minima has been argued (Gerasimovič, 1929) to represent two pulsation modes simultaneously being excited in a 2:1 resonance (for a detailed description, see Pollard et al., 1996). In addition to this short-term behavior, RV Tau variables are divided into two photometric subclasses based on longer-term variability. RVa stars maintain a relatively constant mean magnitude throughout their alternating deep and shallow minima. RVb stars, on the other hand, show an additional long-period variation on a timescale of 600–1500 days in mean magnitude with amplitudes that can reach up to 2 mag in V (Samus et al., 2009).

A major outstanding question in the study of RV Tau stars is the origin of these two classes based on the presence of long-period variation (in their light curves) or lack thereof. Various studies (e.g., van Winckel et al., 1999; Maas et al., 2002; de Ruyter et al., 2005; Gezer et al., 2015; Manick et al., 2017) have argued that RV Tau stars generally can be understood if they possess binary companions. van Winckel et al. (1999) compared various observed characteristics of RV Tau stars with post-AGBs in known binary systems and found that a high fraction of RV Tau stars were similar to their binary post-AGB counterparts. They further suggested that the viewing angle of a

circumstellar dust torus determined the long-term variability class, with RVa stars being seen pole-on and the RVb stars seen edge-on. The RVb long-term variation then is due to periodic extinction by orbiting circumstellar dust. Based on IR excess in the spectral energy distributions (SEDs). indicative of the dust disks of six RV Tau systems, de Ruyter et al. (2005) found that the most likely explanation for the inferred structure and size of the disks is binarity. These studies further support the view that binary companions, and possibly also circumstellar disks, are important for understanding the RV Tau phenomena in general. A binary origin for the RV Tau phenomena would furthermore help to connect RV Tau stars as evolutionary precursors of planetary nebulae, as studies suggest that the asymmetric morphology in the majority of planetary nebulae is also due to binarity (see, e.g., De Marco, 2009).

However, the question of what drives the RVa versus RVb long-term photometric behavior remains. Gezer et al. (2015) used *Wide-field Infrared Survey Explorer (WISE)* data to study all galactic RV Tau stars in the GCVS (Samus et al., 2009) catalog by comparing them to post-AGB objects. They found that all RVb stars in their sample exhibited IR excesses and found them only among the disk sources, whereas some but not all of the RVa stars exhibited such IR excesses. More importantly, they found that all confirmed binaries in their sample were disk sources. Thus, there is evidence that the presence of a dust disk is most strongly connected to the presence of RVb long-term photometric variations in RV Tau stars.

If dust disks cause the signature RVb long-term variation through orbital modulation of the obscuration along the line of sight, then such orbital modulation might be the result of a binary companion, in which case one might expect the modulation to be related to the binary orbital period. In fact, there is evidence for this scenario in RVb stars such as U Mon, an example of a confirmed binary with a dust disk (Gezer et al., 2015), that has a long-term photometric period of 2475 days (Percy et al., 1991) and agrees with the binary orbital period of 2597 days found by Pollard & Cottrell (1995).

Since the discovery of DF Cyg (Harwood, 1927), this archetypal RVb star, which varies in magnitude between $\approx$13–10.5 mag (Bódi et al., 2016), has remained a mystery. Although there

have been some early indications of possible binarity, the radial velocity signature of a binary companion has been inconclusive. For example, Joy (1952) reported a range in the radial velocities of 45 km s^{-1}, measured in 10 plates obtained at Mt. Wilson Observatory, but with a large uncertainty. Moreover, Gezer et al. (2015) classified the SED of DF Cyg as "uncertain" with regards to the evidence for a dust disk.

Fortunately, however, DF Cyg was included in the recent *Kepler* mission, providing an unprecedented high-quality light curve spanning ≈4 years (see Figure 2.1). *Kepler* began observing DF Cyg at the start of a shallow minimum followed by a total of 29 full double-wave (deep + shallow minima) cycles, covering almost two full cycles of an ∼800 day long-term RVb period. In addition, Gorlova et al. (2013) recently reported long-term radial velocity variations with a period of ∼775 days for DF Cyg. Finally, DF Cyg was included in the first data release of parallax observations by *Gaia* (Gaia Collaboration et al., 2016a,b). Together, the *Kepler* light curve and these recent radial velocity and parallax measurements permit a new comprehensive re-evaluation of this important RV Tau system.

In this paper, we present updated measurements of the periodicities in the DF Cyg light curve and show conclusively that DF Cyg possesses a large IR excess indicative of a dust disk. In addition, we present timescale arguments to suggest that the long-term RVb variations in DF Cyg are consistent with a disk obscuration hypothesis on the binary orbital timescale. Section 3.4 summarizes the *Kepler* light curve data that we use in our analysis and Section 2.4 describes our analysis procedures and the main results that emerge from them. We discuss our interpretation of the results in Section 2.5, and conclude with a summary of our findings in Section 2.6.

2.3 Data: *Kepler* Time Series Observations

DF Cyg's brightness variability and that for more than ∼150,000 target stars were simultaneously monitored by *Kepler* through a long time baseline spanning ∼4 years. *Kepler* was designed to survey the Cygnus–Lyra star field region with a 105 degree^2 field of view. A total of 18 observation quarters each lasting ∼90 days were obtained from 2009 May 2 to 2013 April 9 (Q0, Q1, Q8,

and Q17 were approximately 10 days, 33 days, 67 days, and 32 days, respectively). In 2013 May, *Kepler* lost the second of its four reaction wheels, which ended the continuous monitoring mission in the field. However, the observations obtained by *Kepler* provide space-based light curves with the highest photometric accuracy and uninterrupted coverage compared to any ground-based observatory.

Kepler had two observing modes: the short-cadence mode and the long-cadence mode, which took an image (every $\sim$1 minute or every $\sim$30 minutes, respectively) for the duration of the entire mission (Hartig et al., 2014). There are 0.9 – 3 day gaps in the data from the transition of one observing quarter to the next because *Kepler* was required to rotate every three months to maintain direct sunlight on the solar arrays, optimizing their efficiency. Most of the targets fell on a different CCD channel at every observation quarter, and their point-spread functions were distributed among different neighboring pixel apertures. As a result, flux discontinuities exist between quarter-to-quarter transitions.

We retrieved the *Kepler* "simple aperture photometry" (SAP), long-cadence mode data of DF Cyg from the Mikulski Archive for Space Telescopes (MAST). The data are highly sampled in time with a total of $\sim$69,778 data points throughout the 18 observation quarters. Data were collected on day $\sim$120 of the mission and ended at day $\sim$1591, summing to a total of $\sim$4 years of observations.

We use the SAP data as is; however, there were noticeable systematic discontinuities in flux throughout the light curve, due to quarter-to-quarter transitions. We shifted quarters 0–3, 9, and 12 to reduce these discontinuities to best represent the signal of the DF Cyg. These changes were relatively small but helped reduced the error on our measured long-term period value. For an in-depth description on the removal of instrumental effects on *Kepler* data; see, e.g., Hartig et al. (2014).

2.4 Analysis and Results

In this section we present the results of our analysis of the *Kepler* light curve observations of DF Cyg. We give a general characterization of the overall light curve features. We obtain precise

measurements of both the short-term period and long-term period. Finally, we present the results of our analysis of the available broadband flux measurements of DF Cyg, which we use to construct an SED and to estimate the radius of DF Cyg as well as to assess the evidence for a dust disk in the system.

2.4.1 General Features of the DF Cyg Light Curve

Figure 2.1 displays the *Kepler* light curve of DF Cyg. The variations present in the light curve show the characteristic RV Tau alternating minima and a long-period variation in the mean brightness, which are indicative of the RVb classification. *Kepler* observed a complete cycle of the long-period variation, starting as DF Cyg emerged from a long-period minimum and ending as DF Cyg entered a second long-period minimum. As a result, the *Kepler* light curve features two maximum states that bracket one complete minimum state.

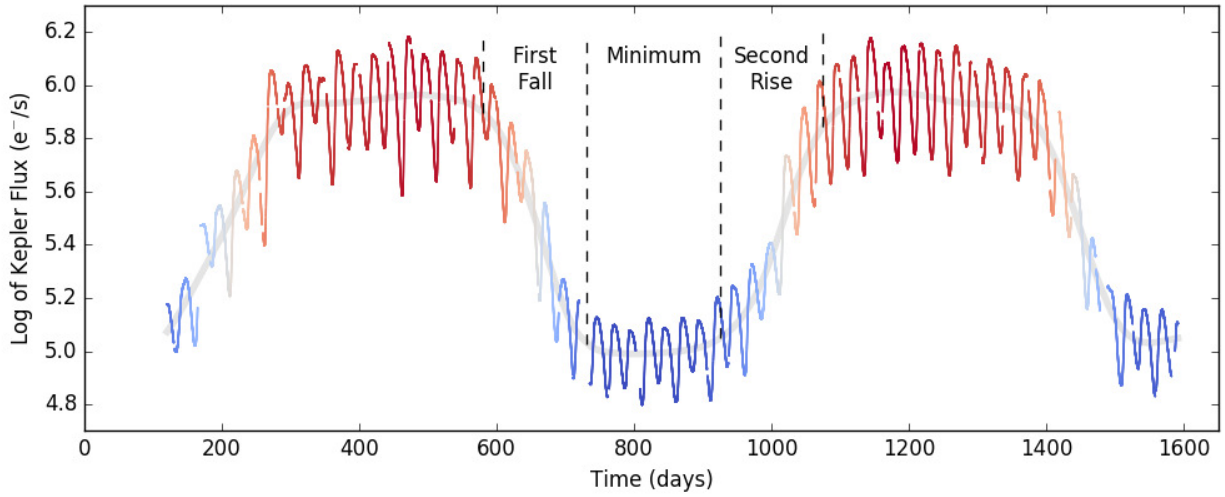

Figure 2.1: *Kepler* light curve for DF Cyg with a spline model (in gray) underlying the long-period trend. The data points are color-coded according to the value of the spline model, where red means maximum light and blue means minimum light. The dashed vertical lines indicate the approximate transitions of light to and from minimum light. Note that the short-term oscillation amplitudes decrease at long-period minimum.

The *Kepler* light curve includes 29 full deep + shallow minima cycles, which we have labeled in Figure 2.2. Both of the long-term maxima are flat with the mean brightness roughly lasting

$\sim$300$\pm$70 days each. The long-term minimum is $\sim$200$\pm$70 days in duration. The long-term brightness rise and fall times are $\sim$150$\pm$70 days each. These general timescales are summarized in Table 2.1. The overall flux decreases by $\sim$90% from the long-period maximum to the long-period minimum. During the long-period maxima, we find that the average peak-to-peak amplitude of the short-period behavior is $\approx 9.2 \times 10^5$ flux units, while in the long-period minimum the average peak-to-peak amplitude is $\approx 7.9 \times 10^4$ flux units. Just as the overall flux decreases by 90%, the short-period oscillation amplitudes decrease by $\sim$90% during the long-period minimum relative to the long-period maximum. In other words, the short-period oscillations are, fractionally, the same during both the long-period maxima and the long-period minimum states. Percy (1993) similarly found that in U Mon, RV Tau, and DF Cyg, the amplitudes of the short-period oscillations get smaller during the long-period minimum. Here, with DF Cyg's *Kepler* light curve, we can clearly see the highly resolved short-period oscillations are $\sim$90% much lower in amplitude during the long-period minima. In Section 2.5, we return to these phenomena in the context of an occultation scenario for DF Cyg.

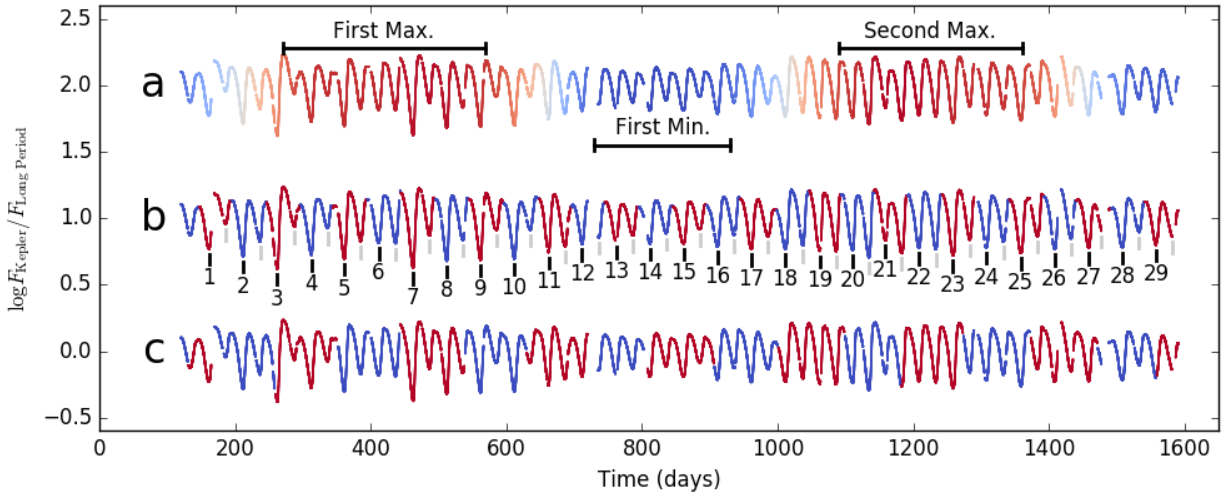

Figure 2.2: *Kepler* light curve for DF Cyg with long-term behavior removed. From top to bottom, we color-code the data according to (a) the value of the long-term behavior spline model, (b) alternating colors based on our double-wave cycle breakdown (there are a total of 29 deep + shallow minima cycles), and (c) alternating colors based on *Kepler* quarters. Location of the extrema of the long (a) and short (b) behaviors are also depicted.

Table 2.1: The long-period transitional behavior of DF Cyg observed by Kepler.

Event	$T_{\rm start}$	$T_{\rm end}$ (Days)	Duration (Days)
First Rise[a]	125 ± 50	275 ± 50	150 ± 70
First Maximum	275 ± 50	575 ± 50	300 ± 70
First Fall	575 ± 50	725 ± 50	150 ± 70
First Minimum	725 ± 50	925 ± 50	200 ± 70
Second Rise	925 ± 50	1075 ± 50	150 ± 70
Second Maximum	1075 ± 50	1375 ± 50	300 ± 70
Second Fall	1375 ± 50	1525 ± 50	150 ± 70

Approximate day on which transitions occur.
[a]The first rise may be incomplete due to the time at which *Kepler* started observing.

2.4.2 Arrival Time Variations in the Deep and Shallow Minima

To verify the periodicity of the short-term behavior in DF Cyg, and to assess any possible variability in the short-term periodicity, we sought to measure the "arrival time" of each light curve minimum. Figure 2.3 shows an example of a deep minimum, Cycle 17, observed by *Kepler*. We fit all 29 deep minima with a Gaussian function, where we used the centroid of the Gaussian, $\mu_{\rm min}$, and its associated error, $\mu_{\rm err}$, to characterize the arrival time of each minimum. Our best-fit arrival time values and associated errors for each deep minimum are presented in Table 2.2 and in Figure 2.4 (top panel), where we show the measured arrival times of each deep minimum as a function of cycle number. We note that the error bars, $\mu_{\rm err}$, are smaller than the data points.

The linear trend of the data indicates the overall consistency of the arrival times of the minima, with a best-fit slope of 49.84 ± 0.02 days, which we take to be the short-term period for DF Cyg. This is consistent with the period of 49.4 days (no quoted uncertainty) originally reported by Harwood (1927), as well as with the recent period reported by Bódi et al. (2016) of 49.9 days.

Subtracting the linear regression from the arrival times gives the residuals, which show systematic deviations, of the arrival times about the best-fit linear trend (Figure 2.4, bottom panel). The deviations are typically on the order of $\sim$0.5 days, with an amplitude of $\sim$2 days. These deviations are highly significant considering the typical uncertainty on the individual arrival times of 0.02 d.

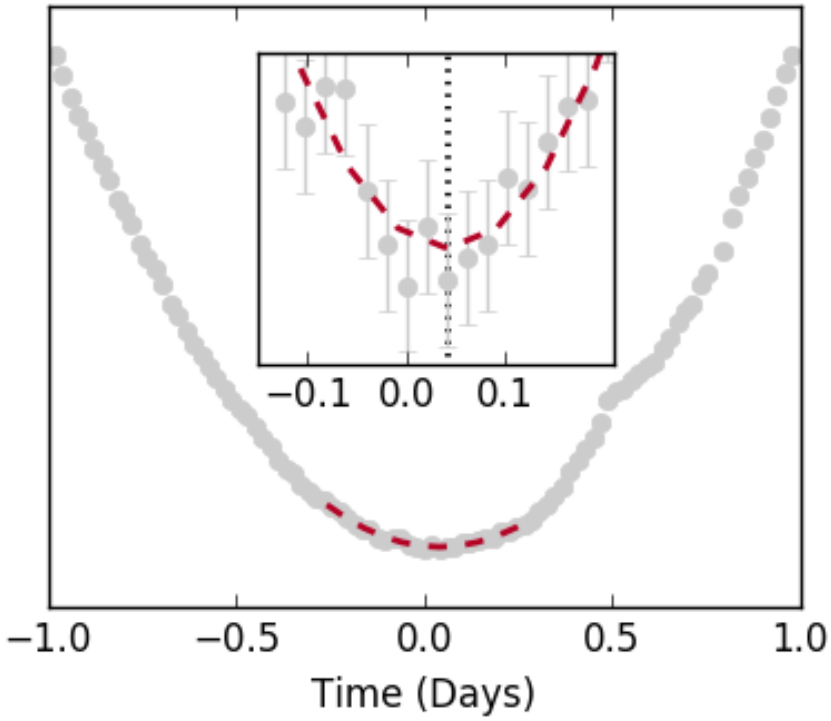

Figure 2.3: Example of arrival time estimate on the deep minimum Cycle 17. The time of the light curve segment is normalized to the time of the data point with the minimum flux. The actual arrival time of the minimum as determined from the Gaussian fit (dashed red line) is indicated by the vertical dotted line shown in the inset zoom.

The pattern of the residuals is not strictly sinusoidal, but does undergo a sign flip (from negative to positive residual) around cycles 4–6 and again (from positive to negative residual) around cycle 21. The timescale between these sign flips, approximately 15–17 cycles, corresponds to a period in the range 747–847 days, given the average short-term cycle period of 49.84 ± 0.02 days found above.

2.4.3 Redetermination of the Long-term Periodicity

DF Cyg's *Kepler* light curve almost spans two full long-period cycles. As an initial estimate, we divided the light curve into two parts at day 800 (Figure 2.5). We heavily smoothed both portions using a spline with a smoothing length of 1150 data points, and cross-correlated the two spline smoothing functions to get a best-fit long-period timescale of 795 ± 5 days. This period is consis-

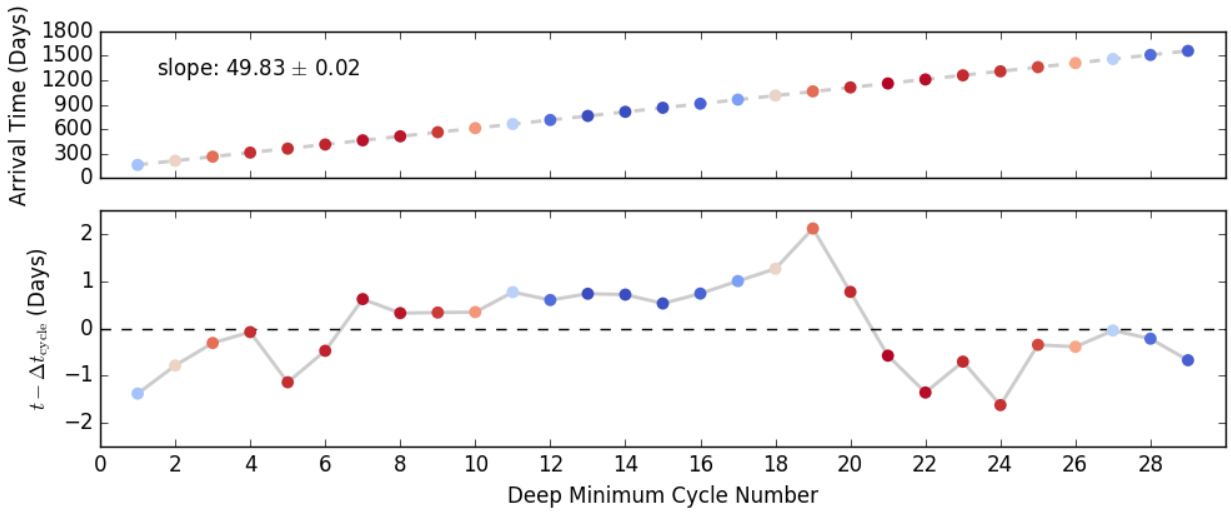

Figure 2.4: Arrival time results. Top panel: the Gaussian-fit arrival times are plotted against the cycle number. The best-fit line to the data is indicated by the dashed line. Lower panel: the residuals of the arrival times and best-fit model are plotted against the cycle number, in the sense of $O-C$ (observed minus calculated). In both panels, the data points are color-coded according to the spline model of the long-period variation, as in Figure 2.1. Errors on the arrival times and on the residuals are smaller than the data points.

tent with previous a estimate (Harwood & Shapley, 1937), and is within 2σ of the 779.6±0.2 day value reported by Bódi et al. (2016) from 50 years of AAVSO measurements.

We note that a period of ∼800 days is almost exactly 16 times the short period we found above of 49.84 ± 0.02 days, which would correspond to a long period of 797.4±0.3 days. Long-to-short period ratios of this order are generally observed in other RVb stars (Tsesevich, 1975; Percy, 1993). When we phased the *Kepler* light curve by this long-period value (Figure 2.5), the arrival times of the short-period oscillations align well. However, the amplitudes do differ, indicating that the variations in the system are not strictly periodic in every detail. At the same time, the long-period behavior does show broad repeatability at this period, especially in the alignment of the rises to long-period maxima and the descents toward long-period minima. In addition, the flux at long-period maxima are both flat. The flat long-period maxima and their different durations resemble the RVb binary, U Mon (Percy, 1993). Overall, we remark that the long-term periodic behavior is reminiscent of an eclipsing binary. We return to the idea of a periodic occultation hypothesis in

Table 2.2: The deep minima arrival time of DF Cyg in the Kepler light curve.

Cycle Number	Arrival Time (Days)	Lag Time (Days)
1	161.628 ± 0.003	-1.43 ± 0.020
2	212.059 ± 0.002	-0.83 ± 0.020
3	262.372 ± 0.001	-0.35 ± 0.020
4	312.438 ± 0.001	-0.12 ± 0.020
5	361.214 ± 0.001	-1.18 ± 0.020
6	411.716 ± 0.001	-0.51 ± 0.020
7	462.645 ± 0.002	0.58 ± 0.020
8	512.185 ± 0.001	0.29 ± 0.020
9	562.033 ± 0.001	0.30 ± 0.020
10	611.880 ± 0.002	0.31 ± 0.020
11	662.138 ± 0.001	0.73 ± 0.020
12	711.808 ± 0.002	0.57 ± 0.020
13	761.780 ± 0.006	0.71 ± 0.021
14	811.595 ± 0.006	0.69 ± 0.021
15	861.244 ± 0.005	0.50 ± 0.020
16	911.290 ± 0.008	0.71 ± 0.021
17	961.392 ± 0.007	0.98 ± 0.021
18	1011.488 ± 0.003	1.24 ± 0.020
19	1062.175 ± 0.002	2.09 ± 0.020
20	1110.671 ± 0.001	0.75 ± 0.020
21	1159.160 ± 0.003	-0.59 ± 0.020
22	1208.217 ± 0.001	-1.37 ± 0.020
23	1258.706 ± 0.001	-0.72 ± 0.020
24	1307.624 ± 0.002	-1.63 ± 0.020
25	1358.736 ± 0.002	-0.36 ± 0.020
26	1408.529 ± 0.002	-0.40 ± 0.020
27	1458.711 ± 0.002	-0.05 ± 0.020
28	1508.374 ± 0.006	-0.22 ± 0.021
29	1557.755 ± 0.005	-0.68 ± 0.020

Gaussian-fit arrival time for each deep minimum cycle and residuals plotted in Figure 2.3.

Section 2.5.

Finally, we noticed that at both of the long-period maxima, the pattern of deep and shallow minima becomes temporarily interrupted. Specifically, the shallow minimum of Cycle 5 and the subsequent deep minimum of Cycle 6 (at day $\sim$400) have roughly the same absolute flux and are not as readily distinguishable as deep versus shallow. The same occurs for the shallow minimum of Cycle 21 and the subsequent deep minimum of Cycle 22 (at day $\sim$1200; Figure 2.2). These temporary interruptions coincide with the sign reversals in the arrival time residuals observed in

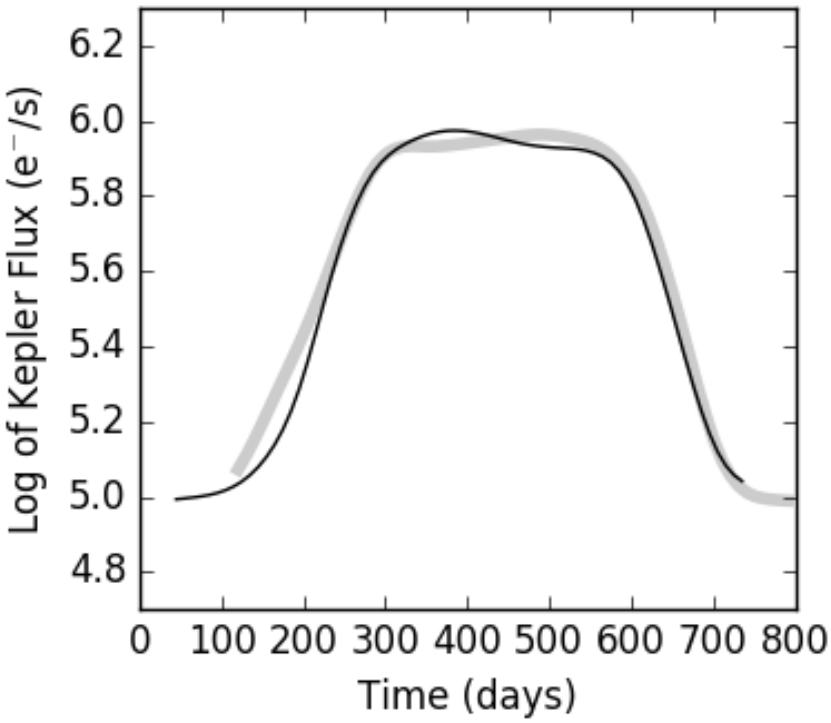

Figure 2.5: Phasing the Long-period spline. The gray curve represents the first half of the long-period cycle determined from the spline model described in the text. The black curve represents the second half of the long-period cycle phased by 795-d. Phases greater than ± 5 days can be disregarded, giving the best-fit long-term period of 795 ± 5 days.

Section 2.4.2 and Figure 2.4, a behavior separated by $\sim$800 days.

2.4.4 SED: Stellar Radius and Dust Disk

We gathered the available broadband photometric data for DF Cyg from *GALEX*, *Tycho-2*, *APASS*, *2MASS*, and *WISE* to produce the observed SED spanning the wavelength range 0.2–20 μm as shown in Figure 2.6. We used an adopted effective temperature of $T_{\rm eff} = 4840$ K (Giridhar et al., 2005; Brown et al., 2011; Bódi et al., 2016). The 2MASS fluxes are clearly anomalous, and we confirmed from the timestamps in the 2MASS catalog that this is due to the 2MASS observations of DF Cyg having been taken near minimum brightness of the star (Skrutskie et al., 2006). In addition, the *WISE* bands exhibit a clear excess. Therefore, we attempted a fit to only the portion of the SED at $\lambda < 1$ μm. The UV to optical portion of the SED can be explained with a Kurucz

stellar atmosphere model (we adopt solar metallicity for simplicity) with a best-fit extinction of $A_V = 0.61 \pm 0.06$ mag, implying a distance of $\sim$1.3 kpc for this sightline based on the 3D dust maps of Green et al. (2015). Indeed, the newly available *Gaia* parallax of $\pi = 1.01 \pm 0.38$ mas puts DF Cyg at 990 ± 372 pc.

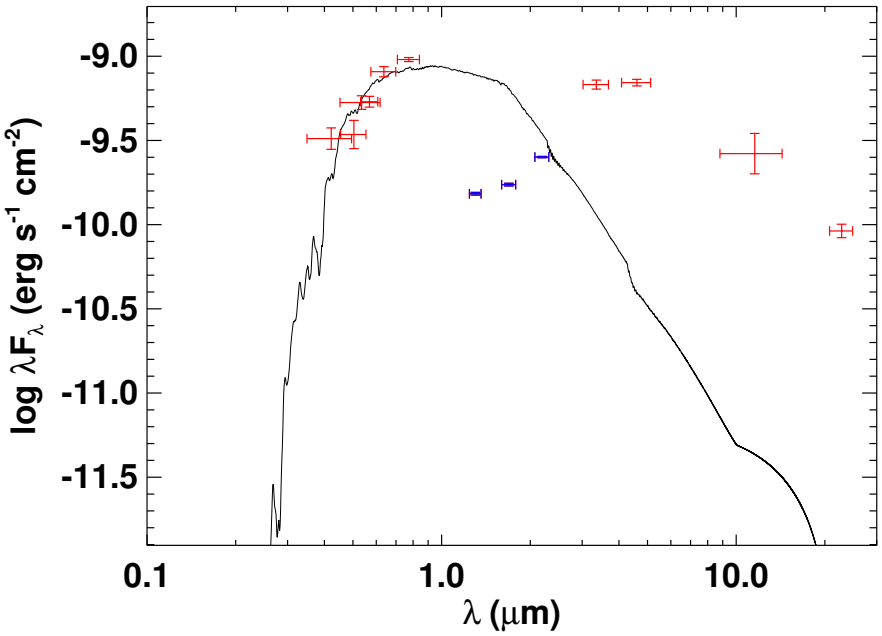

Figure 2.6: SED with our best-fitting stellar atmosphere model to the optical photometry (black line). Measured fluxes are shown as red crosses where the vertical bars represent the measurement uncertainties and the horizontal bars represent the width of the passband. The aberrant 2MASS JHK_S photometry (blue data points) is due to those observations having been taken during an RVb dimming of DF Cyg. The *WISE* measurements reveal a clear and strong infrared excess, typically indicative of a dusty disk (see the text).

Integrating the model SED for the DF Cyg photosphere (black curve in Figure 2.6) gives a (dereddened) bolometric flux at Earth of $F_{\rm bol} = 1.71 \pm 0.05 \times 10^{-9}$ erg s^{-1} cm^{-2}. With $T_{\rm eff} =$ 4840 K (see above), this yields an angular radius of $\Theta = 0.048 \pm 0.001$ mas. Using this calculated angular radius with the *Gaia* distance in turn yields a physical radius for DF Cyg of $R_\star = 10.3 \pm 3.8$ R$_\odot$, consistent with an evolved status for DF Cyg. We note that this radius is somewhat smaller than is typically found for RV Tau stars using period–luminosity–color relations (e.g., Manick et al., 2017).

In addition, there is a large IR excess evident from the *WISE* data, consistent with that expected

from a dusty circumstellar disk ((Gezer et al., 2015); disk model discussed in Section 2.5). The IR excess was not conclusive in the study of Gezer et al. (2015) because the *WISE* data alone exhibit a combination of [3.4]−[4.6] and [12]−[22] colors that placed DF Cyg just at the edge of their "disk" criterion. Here, the inclusion of the full SED makes the detection of a large IR excess indicative of a disk unambiguous. In comparison, the 2MASS JHK_S measurements appear anomalously low. However, we note that the 2MASS observations were obtained during a long-period minimum state (1998 June 13), with a phase corresponding to day ∼800 in Figure 2.1. These measurements are further discussed in Section 2.5.

2.5 Discussion: Disk Occultation Scenario for the Long-period Behavior

In this section, we discuss the stellar parameters we obtained for DF Cyg, such as periodicity, the residual trend from the short-period minima arrival times, as well as its radius and the confirmation of its IR excess. We develop a scenario in which DF Cyg and its binary companion undergo periodic occultations by a dusty circumbinary disk.

2.5.1 Evidence for a Binary Companion with an 800 Day Period

There is now strong evidence to suggest the presence of a binary companion orbiting DF Cyg with a period of ∼800 days. Gorlova et al. (2013) reported preliminary results from a long-term radial velocity monitoring program of ∼70 supergiants that included post-AGB stars with disk detections. They found DF Cyg to be one of their best binary candidates, with a period of ∼775 days (no uncertainty reported). Some of the other candidates include EP Lyr (∼1100 days), R Sge (≈1159 days), and RV Tau (≈1210 days). All of these are RVb stars with previously recorded long-term photometric periods ranging from ∼1100–1200 days (e.g., Evans, 1985; Gielen et al., 2009a).

In the case of DF Cyg specifically, if we assume a circular Keplerian orbit for the binary companion and adopt a typical post-AGB mass of 0.6 $M_\odot$ for the mass of DF Cyg (Weidemann, 1990), we obtain a range of semi-major axis values depending on the assumed mass of the companion.

For example, for companion masses in the range 1–3 $M_{\odot}$, we obtain a range of semimajor axis $a \approx$ 1.5–2.5 AU.

Importantly, all of the previously identified RVb stars with binary companions appear to also possess dusty disks, based on their SEDs (Gorlova et al., 2013; Gezer et al., 2015). In addition, Manick et al. (2017) reported that all six of the RV Tau stars in their radial velocity study have disks and have binary companions with orbital periods of 650–1700 days and eccentricities of 0.2–0.6. Therefore, in both of these larger samples of RV Tau stars, there appears to be a connection between the presence of a binary companion, the signatures of dusty disk material, and the periods of both the binary orbit and the long-period photometric "RVb" variation.

Similarly, our results for the behavior in the short-period oscillation arrival times (Section 2.4) suggest that DF Cyg undergoes some sort of perturbation with a period comparable to the long-period "RVb" oscillation of 795 ± 5 days, which is itself comparable to the binary companion period of $\sim$775 days reported by Gorlova et al. (2013). A phenomenon related to heartbeat stars (Thompson et al., 2012), whose tidal distortions at periastron introduce periodic variations in the light curve, could be related to the temporary interruptions of the deep and shallow minima.

This confluence of variability timescales—all around $\sim$800 days—motivates us to consider a unifying interpretation involving the binary companion and a dusty disk in the circumbinary environment of DF Cyg, as we now discuss.

2.5.2 Disk Occultation Scenario

We begin by ruling out the possibility of having only a simple eclipsing binary star scenario, in which the $\sim$90% decrease in light during the long-period minimum is caused by DF Cyg eclipsing a hot, luminous companion that contributes $\sim$90% of the total system light. First, the duration of the long-period "RVb" dimming is very long—about half of the orbital period. It is very difficult to construct an orbital configuration in which a companion star can spend half of the orbit traversing behind DF Cyg. Perhaps this could occur if the orbit is highly eccentric; however, the orientation of the orbit would have to be fortuitously aligned with our line of sight, such that the companion

is being blocked at apastron to account for the very long duration it would then spend in eclipse.

Second, in this scenario, we would expect a secondary eclipse to occur at periastron as the companion passes in front of DF Cyg. However, we do not see any signs of a secondary eclipse in the light curve near the phases of the long-period maxima. Finally, since the short-period oscillations are observed to decrease by $\sim$90% in amplitude during the long-period minimum, it must almost certainly be the case that it is DF Cyg that is principally occulted during long-period minima. This instead requires that $\sim$90% of the stellar disc of DF Cyg is obscured by a very large, opaque screen.

If we instead interpret the long-period changes in average flux to be due to ingresses, eclipse, and egresses of an opaque body passing in front the DF Cyg + companion system, we can attempt to characterize the occulting body. Given that DF Cyg exhibits a clear IR excess indicative of a dusty disk somewhere in the system, one interpretation is that the occulting screen is a feature in a disk around DF Cyg itself or else a disk around the companion star. Therefore, we first consider the approach laid out in Rodriguez et al. (2013) for the occultation of a star by an orbiting disk. The extent of the screen can be obtained by calculating its transverse velocity, using our empirically obtained radius for DF Cyg and the duration of ingress (or egress). We calculated the size, w, of the occulting screen from the screen's transverse velocity, $v_{\rm T}$, and the amount of time, $t_{\rm eclipse}$, given by the sum of the ingress duration and the total eclipse duration, $t_{\rm eclipse} = w/v_{\rm T}$. The transverse velocity is itself related to the size of DF Cyg and the ingress duration, $t_{\rm ingress}$, by $v_{\rm T} = 2R_{\star}/t_{\rm ingress}$, where $R_{\star}$ is the radius of DF Cyg. Thus, $w = 2R_{\star}t_{\rm eclipse}/t_{\rm ingress}$. With an observed $t_{\rm ingress}$ = 150 $\pm$ 70 days and observed $t_{\rm eclipse}$ = 350 $\pm$ 70 days, we obtain $v_{\rm T}$ = 1.11 $\pm$ 0.66 km s^{-1} and $w = 0.22 \pm$ 0.14 AU.

We considered two possibilities for the location of the dusty disk occulting DF Cyg and producing dimmings, in the context of the above scenario from Rodriguez et al. (2013): (1) a circumstellar disk around DF Cyg itself, and (2) a circumstellar disk around a companion star, and this companion/disk system periodically occulting DF Cyg. However, neither of these is geometrically convincing. First, to not occult DF Cyg during half of the cycle but then occult $\sim$90% of DF Cyg

during the other half of the cycle, a disk around DF Cyg would need to have a very "tall" feature or warp on one side. Given the radius of DF Cyg ($\approx$10.3 $R_\odot$), this warp would need to extend vertically by $\sim$10 $R_\odot$; with an inferred total disk extent of $\sim$0.2 AU, or $\sim$50 $R_\odot$, this would be a remarkably large perturbation indeed. On the other hand, to periodically occult DF Cyg with a period equal to the orbital period of the companion star, and assuming a Keplerian disk, the disk warp would need to be located at the same distance as the companion star. However, it would then presumably not be possible for the disk to remain stable if it completely fills the binary orbit.

The second possibility, in which the binary companion is encircled by a dusty disk, and it is the binary companion/disk system that periodically occults DF Cyg at the binary orbital period, is also geometrically impossible. Specifically, based on the fraction of the total light curve duration that the dimming event spans, the binary companion and its disk would need to spend roughly half of the orbital period in front of DF Cyg, leaving half of the orbital period for the binary to traverse all other orbital phases. Even imagining that the companion is on a highly eccentric orbit and that the orbit is moreover fortuitously aligned with the observer such that the occultations correspond to apastron, it is not geometrically possible to explain the occultation durations relative to the entire orbit in such a scenario.

Thus, we are led to conclude that the opaque screen periodically occulting DF Cyg is a circumbinary dusty disk around an entire binary system. This would represent an interpretation similar to that described in Gorlova et al. (2015) for the IRAS 19135+3937 interacting binary system (see their Figure 18), although much simpler in this case as there is no evidence in DF Cyg for the additional complexities of accretion, jets, or any reflection effects.

By adopting the interpretation that an opaque disk periodically occults DF Cyg, we therefore infer that the 2MASS JHK_S measurements, which were obtained during the long-period minimum (Section 2.4.4), are a combination of infrared flux from the disk plus the unobscured part of the photosphere of DF Cyg[1]. If we assume that the stellar SED model in Figure 2.6 represents the

[1] We ignore any contribution from the binary companion, which is presumably very faint in the visible in comparison to DF Cyg. This assumption is corroborated by the fact that the radial velocity monitoring of DF Cyg that identified the orbital motion of DF Cyg did not observe the spectrum of the companion (Gorlova et al., 2013).

expected flux from the full photosphere, we can use the 2MASS measurements to isolate the JHK_S flux of the disk alone. To do this, we estimated the "undimmed" 2MASS JHK_S fluxes by interpolating from a straight line in Figure 2.6 between the 0.8 and 3.5 μm measurements. The resulting ratio of the dimmed to the undimmed flux at JHK_S is $\sim$0.19, $\sim$0.22, and $\sim$0.33, respectively.

These ratios indicate greater dimming at shorter wavelengths, which could be interpreted as interstellar-like extinction if the occulting disk is semi-transparent. Therefore, we compared these flux ratios, as a function of wavelength, to an extinction model based on the Cardelli et al. (1989) interstellar extinction law. In this comparison, we normalized the extinction law to the $\sim$0.10 flux ratio we measured from DF Cyg's *Kepler* light curve, adopting the midpoint of 0.66 μm for the *Kepler* bandpass. We found that the JHK_S flux ratios are dimmer than that expected from the interstellar extinction law. Alternatively, if the occulting disk is opaque and black (i.e., non-emitting), we would expect the dimming to be gray. However, the flux ratios measured above are not gray. Rather, the trend from the *Kepler* and JHK_S flux ratios falls in between the two extreme cases of interstellar-like extinction and an opaque non-emitting disk, suggesting that the occulting screen is opaque but also glowing in the near-IR.

To test for a glowing disk, we attempted to estimate how bright the 2MASS data points would have been had they been measured at the long-period maximum state. If the observed 2MASS measurements come from 10% of the DF Cyg photosphere and 100% of the disk, the relation between the fluxes is described by

$$F_{2MASS} = 0.1F_{DFCyg} + F_{Disk}, \tag{2.1}$$

and the total flux expected at the long-period maximum is given by

$$F_{Total} = F_{DFCyg} + F_{Disk}. \tag{2.2}$$

Here, F_{2MASS} is the 2MASS flux measurement, F_{DFCyg} is the flux of DF Cyg, which we estimated from our SED photosphere model, and F_{Disk} is the flux of the disk. By solving equations 1 and 2

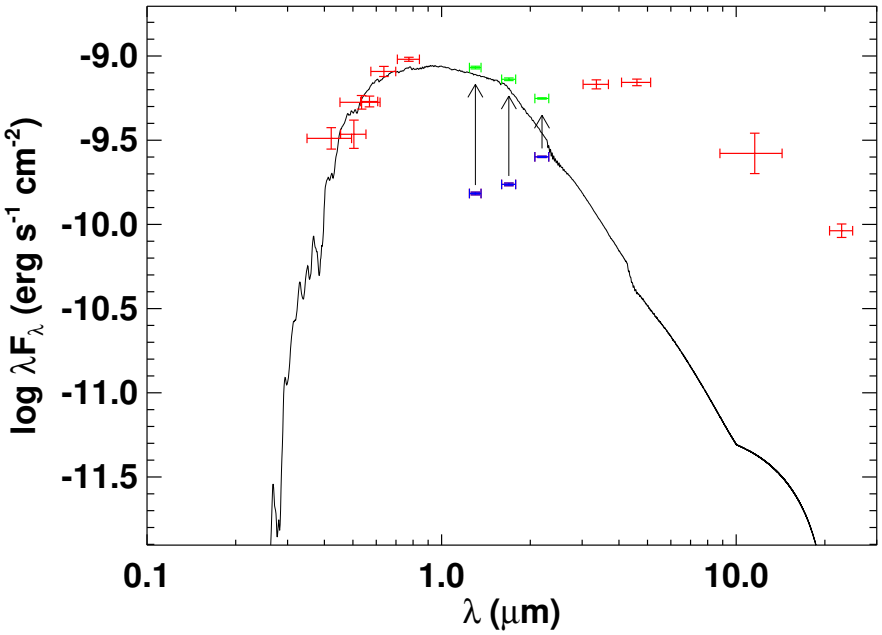

Figure 2.7: Same as Figure 2.6, but now including the JHK_S fluxes corrected upward (arrows pointing to green symbols) for the obscuration of the luminous, occulting disk (see the text).

for each 2MASS JHK_S bandpass individually, we find total fluxes of $10^{-9.0}$, $10^{-9.09}$, and $10^{-9.2}$ erg s^{-1} cm^{-2}, respectively. These values increase the originally measured 2MASS points, as shown in Figure 2.7, now revealing a double-peaked SED. Such a double-peaked SED is similar to that of other RV Tau stars with disks (see, e.g., de Ruyter et al., 2005), lending additional credibility to the occulting disk scenario. From the shape of the SED, we estimate that the disk peaks at $\sim 3.5-4\mu m$. Using Wien's displacement law we can then estimate the temperature (of the inner edge) of the disk to be $\sim$770 K.

Studies such by de Ruyter et al. (2005, 2006) have previously suggested that dusty disks, possibly circumbinary disks, around RV Tau and post-AGB stars can be stable over long timescales. A few recent studies provide more compelling evidence for dusty circumbinary disks around post-AGB and RV Tau stars (Gielen et al., 2009b; Hillen et al., 2014, 2015). Gielen et al. (2009b) used SED modeling of four RV Tau stars and inferred dusty disks around them. They moreover found that the disks were likely to be puffed up, i.e., having large scale heights. They also determined that these disks possess inner holes, where the inner disk radii are typically a few astronomical

units, similar to the semimajor axis that we derive above for the DF Cyg binary orbit.

Hillen et al. (2014) used interferometric measurements and SED fitting to similarly infer a puffed-up circumbinary disk with an inner hole around the binary post-AGB star 89 Her. The inferred disk scale height in that system suggests that a partial blocking of the central star should occur for ∼20-30% of viewing angles. This fraction is also consistent with occurrence rates of RVb stars. For example, GCVS currently has 159 RV Tau stars on record, 45 classified as RVa's and 19 classified as RVb's (the rest are not listed with a classification), giving an RVb occurrence of 30% among the classified systems.

Note that this interpretation requires that some RVa-type stars also have disks but that these be viewed from more pole-on orientations such that the central RV Tau star is not obscured. van Winckel et al. (1999) was the first to suggest viewing angle and variable circumstellar extinction determined the RV Tau's photometric class. Indeed there are known examples of such systems. For example, AC Her, an RVa pulsator (no long-period dimming events) is in a confirmed binary system (van Winckel et al., 1998) surrounded by a stable circumbinary disk. Hillen et al. (2015) recently found evidence that AC Her's circumbinary disk is puffed up with a large inner disk radius.

2.6 Summary and Conclusions

We have studied the *Kepler* light curve of the RV Tau variable DF Cyg with unprecedented photometric and temporal resolution. We determined that the characteristic RV Tau variable short-term pulsation has a period of 49.84 ± 0.02 days and the RVb longer-term variation has a period of 795 ± 5 days, which are consistent with period values in the literature. We found that the overall mean flux decreases by ∼90% from the long-period maxima to the long-period minimum and that the short-period peak-to-peak amplitudes, during long-period maxima, also decrease by ∼90% at long-period minimum.

During the maxima of the long-period behavior, we identified two temporary interruptions of the deep and shallow minima occurring on the order of ∼800 days. Studying the residuals of the arrival times for the deep minima, we discovered a similar trend on the order of ∼800 days.

A previously measured radial velocity period of $\sim$775 days suggests an orbital period consistent with the $\sim$800 day features present in the light curve.

Hence, there is compelling and corroborative evidence to associate the long-period variation and other $\sim$800 day features with a binary orbital period. It has also been suggested that the long-period behavior in RVb stars is due to the geometry of circumstellar disks where the stars are periodically occulted by their disks. Using DF Cyg's stellar parameters, based on the recent *Gaia* parallax measurement, and our analysis of the *Kepler* light curve, we considered such a scenario for DF Cyg.

We argue that if the periodic long-term behavior is due to orbital modulation by an opaque body that blocks $\sim$ 90% DF Cyg + companion's light, then the only feasible configuration is a puffed-up circumbinary dusty disk surrounding the DF Cyg system. Such a scenario is consistent with DF Cyg's IR excess, which suggests the presence of a dusty disk. This interpretation is bolstered by our analysis of the 2MASS JHK_S observations (taken during long-period minimum), which indicates the presence of a double-peaked SED in the near-IR similar to that of other RV Tau stars. This, in turn, suggests that the disk occultation scenario advanced here may apply generally to RVb-type variables.

Chapter 3

Multiwavelength Observations of the RV Tauri Variable System U Monocerotis: Long-Term Variability Phenomena That Can Be Explained by Binary Interactions with a Circumbinary Disk

The following work was originally published in The Astrophysical Journal (Vega et al., 2021) and is reprinted below in its entirety.[1]

Laura D. Vega[1,2,*], Keivan G. Stassun[1], Rodolfo Montez Jr.[3], Tomasz Kamiński[4], Laurence Sabin[5], Eric M. Schlegel[6], Wouter H. T. Vlemmings[7], Joel H. Kastner[8], Sofia Ramstedt[9], Patricia T. Boyd[2]

[1]Department of Physics & Astronomy, Vanderbilt University, Nashville, TN, USA

[2]Astrophysics Science Division, NASA Goddard Space Flight Center, Greenbelt, MD, USA

[3]Center for Astrophysics | Harvard & Smithsonian, Cambridge, MA, USA

[4]Nicolaus Copernicus Astronomical Center of the Polish Academy of Sciences, Toruń, Poland

[5]Instituto de Astronomía, Universidad Nacional Autónoma de México, Ensenada, B. C., México

[6]Department of Physics & Astronomy, The University of Texas at San Antonio, San Antonio, TX, USA

[7]Department of Space, Earth and Environment, Chalmers University of Technology, Onsala Space Observatory, Onsala, Sweden

[8]School of Physics and Astronomy, Rochester Institute of Technology, Rochester, NY, USA

[9]Department of Physics and Astronomy, Uppsala University, Uppsala, Sweden

[*]NASA MUREP Harriett G. Jenkins Predoctoral Fellow

[*]Fisk-Vanderbilt Master's-to-PhD Bridge Program

[1] A NASA news feature was published for this research: https://www.nasa.gov/feature/goddard/2021/scientists-sketch-aged-star-system-using-over-a-century-of-observations

3.1 Original Abstract

We present X-ray through submillimeter observations of the classical RV Tauri (RVb-type) variable U Mon, a post-AGB binary with a circumbinary disk (CBD). Our SMA observations indicate a CBD diameter of $\lesssim 550$ au. Our XMM-Newton observations make U Mon the first RV Tauri variable detected in X-rays. The X-ray emission is characteristic of a hot plasma (~ 10 MK), with $L_X = 5 \times 10^{30}$ erg s^{-1}, and we consider its possible origin from U Mon, its companion, and/or binary system interactions. Combining DASCH and AAVSO data, we extend the time-series photometric baseline back to the late 1880s and find evidence that U Mon has secular changes that appear to recur on a timescale of ~ 60 yr, possibly caused by a feature in the CBD. From literature radial velocities we find that the binary companion is a ~ 2 M$_\odot$ A-type main-sequence star. The orientation of the binary's orbit lies along our line of sight ($\omega = 95^\circ$), such that apastron corresponds to photometric RVb minima, consistent with the post-AGB star becoming obscured by the near side of the CBD. In addition, we find the size of the inner-CBD hole (~ 4.5–9 au) to be comparable to the binary separation, implying that one or both stars may interact with the CBD at apastron. The obscuration of the post-AGB star implicates the companion as the likely source of the enhanced Hα observed at RVb minima and of the X-ray emission that may arise from accreted material.

3.2 Introduction

RV Tauri-type variable stars are F through K supergiants with luminosity classes between Ia and II. They extend the brightest part of the Type II Cepheid (i.e., RR Lyr, BL Her, W Vir, and RV Tau stars) instability strip on the H-R diagram, as well as the brightest part of their period-luminosity relation, with radial pulsation periods longer than 20 days (Soszyński et al., 2017). However, it has been shown that RV Tauri variables follow a steeper period-luminosity relation compared to their shorter-period Type II Cepheid counterparts (e.g. Bódi & Kiss, 2019).

The signature characteristic of RV Tauri variables are the alternating deep and shallow minima in their light curves: the time between a deep minimum and its successive shallower minimum is called the "fundamental" period; the time between two successive deep minima is the "formal" period. The alternation of deep and shallow minima is not strict in nature, as the light curves also show strong cycle-to-cycle variability, where the depths of the minima can vary randomly and may be attributed to low-dimensional chaotic behavior (e.g. Plachy et al., 2014, 2018, and references therein). In addition to pulsations, a photometric subgroup (RVb-type) displays an additional, slower, periodic variation in mean brightness that ranges between 470 and 2800 days (Soszyński et al., 2017). There are $\sim$ 300 identified RV Tauri variables in the Galaxy (Soszyński et al., 2020).

It has been established that most RV Tauri variables are a subclass of post-asymptotic giant branch (post-AGB) stars in binary systems surrounded by a dusty circumbinary disk (CBD), and there is argument for the companion to be an unevolved main-sequence star (van Winckel et al., 2009; Manick et al., 2019). The post-AGB primary is evolved from a low-to-intermediate-mass progenitor (0.8–8 $M_\odot$), on their way to forming a planetary nebula, based on high luminosities ($\sim 10^3$–10^4 $L_\odot$), mass-loss history, and infrared excess (indicative of dust) in their spectral energy distribution (SED; Gehrz, 1972; Evans, 1985; Jura, 1986; Alcock et al., 1998; van Winckel, 2003). Groenewegen & Jurkovic (2017) recently found mass estimates for RV Tauri variables in the Magellanic Clouds that showed either very high ($\gtrsim 1$ $M_\odot$) or very low mass values ($\lesssim 0.5$ $M_\odot$), which are in conflict with the standard single-star evolution of a post-AGB object, likely due to different evolutionary channels and perhaps revealing the effects of binarity. It may be that some of these

post-AGB systems may evolve too slowly to ever become planetary nebulae (van Winckel, 2017). Bódi & Kiss (2019) showed similar mass estimate results to those of Groenewegen & Jurkovic (2017), for a small sample of Galactic RV Tauri variables.

It was recently discovered that some of the less luminous RV Tauri variables are actually post-red giant branch (post-RGB) stars, a class of objects that have similar spectroscopic stellar parameters to their post-AGB counterparts but appear at lower luminosities on the H-R diagram (Kamath et al., 2016; Manick et al., 2018). These objects are thought to have evolved off the RGB instead of the AGB as a result of binary interaction.

The CBDs around post-AGB (and post-RGB) binaries are described as second-generation 'scaled-up' analogs to proto-planetary disks surrounding young stellar objects (YSOs; Hillen et al., 2017; van Winckel, 2018). The near-IR excess observed in the SEDs of these bright post-AGB binaries, especially the RV Tauri variables, comes from hot dust close to the central source, where a disk-like nature of the near-IR emission has been confirmed by interferometric observations (Deroo et al., 2006). The mid- to far-IR excess then comes from cooler dust in the disk (de Ruyter et al., 2006; Hillen et al., 2015).

The CBDs are found to be relatively compact with sufficient angular momentum, in combination with the binary system's gravity, to settle and form the rotating disk from ejected material, especially from the huge mass loss after the AGB phase (up to 10^{-4} $M_{\odot}$ yr^{-1}) of the evolved primary (Bujarrabal et al., 2013). Keplerian rotation of the circumbinary material around these stars has been resolved by narrow CO line profiles, as well as the presence of large grains with a high degree of crystallinity, indicating longevity and stability, that form these disks (Gielen et al., 2011) with diameters ranging between $\sim$ 100 and 2000 au (Bujarrabal et al., 2005, 2013, 2018).

The slower photometric phenomenon from the RVb subset of RV Tauri systems (and in other post-AGB binaries) has been attributed to an extrinsic variable extinction. An inclined CBD can shadow the primary at certain phases of its orbit (e.g., Manick et al., 2017), blocking the light, and causing extinction and scattering along our line of sight. Vega et al. (2017) used ultra-precise flux measurements from the *Kepler* telescope and found that the decrease in pulsation amplitude of

DF Cyg (the only RV Tauri system in *Kepler*'s original field of view) perfectly tracked the decrease in flux from its RVb oscillation, showing that the long-term minima are due to the disk obscuring the pulsating primary. Kiss & Bódi (2017) further extended this study to all known RVbs in the Galaxy (by also adopting flux units instead of the inverse logarithmic magnitude system) to confirm that all RVbs displayed the correlation found in DF Cyg. Furthermore, by using interferometric observations, Kluska et al. (2019) have found that the RVb sources in their sample have high inclinations, implying a very high disk scale height and allowing the disk-shadowing interpretation to be correct.

The presence of disks has also been linked to the phenomenon known as depletion, which is found in post-AGB binaries. Depletion is a systematic under-abundance of refractory elements, in the photospheres of post-AGB stars, that correlates with the condensation temperature of an element (Giridhar et al., 2000). In order to get a depleted photosphere, the stellar radiation pressure on circumstellar material separates dust grains (containing refractory elements) from the volatile-rich gas that gets reaccreted onto the stellar surface. Since dust grains experience a much larger radiation pressure, they do not get accreted. Depletion is thought to be caused by accretion of metal-poor gas from the CBD (Waters et al., 1992). Even though the presence of a disk seems to be needed, it is not a sufficient condition for depletion to occur since not all post-AGB binaries with disks are depleted (Gezer et al., 2015).

Though it is clear that binarity plays a very important role in the dynamics and evolution of post-AGB systems, the details of binary interaction processes are still not well understood (van Winckel, 2018) and have been an important topic of investigation. New advances on the discovery of high-velocity outflows in post-AGB binaries have brought to light unique orbital phase-dependent variations in the Hα profiles and have proven to be rather common in post-AGB binaries (Gorlova et al., 2012, 2014, 2015; Bollen et al., 2017, 2019, 2020). Studies associate this phenomenon with binary interaction and show that these high-velocity outflows (i.e. a bipolar jet) are launched by an accretion disk around the companion (i.e. circumcompanion accretion disk) that produces a P Cygni profile from the Hα emission line, as the jet from the companion transits

the bright post-AGB primary. Based on accretion models for two well-sampled post-AGB binaries, Bollen et al. (2020) concluded that the CBD is likely feeding a circumcompanion accretion disk. This agrees with the observed depletion patterns of refractory elements in post-AGB binaries (Oomen et al., 2020). Manick et al. (2019) have already shown similar Hα variations that point to the presence of jets for two RV Tauri systems: RV Tau and DF Cyg.

In the context of the recent developments in the field of post-AGB binaries, we report new observations that may provide insight into how binarity plays a role in these systems. In this paper we present the most comprehensive, multiwavelength analysis to date of a classical RVb variable: U Monocerotis (U Mon). The analysis includes an X-ray detection—never before reported for any RV Tauri system—and an unprecedented photometric time series spanning 130 yr. Our results focus on consolidating several characteristics displayed in previous measurements, such as the very long time baseline photometry. We introduce recent space- and ground-based data collected for U Mon from the XMM-Newton X-ray satellite and the Submillimeter Array (SMA), respectively.

We give an introduction to the U Mon system in Section 3.3 and describe each data set in Section 3.4. We present our results in Section 3.5, including evidence for an even longer-term secular variation in the U Mon light curve that may recur every $\sim$ 60 yr and that may represent a persistent feature in the U Mon CBD; a refined determination of the disk's inner hole, which appears to coincide with the size of the binary orbit; a new characterization of the binary companion star; and evidence for its possible interaction with the CBD's inner edge. In Section 3.6 we discuss the implications of our findings and present U Mon as a template for the discovery of X-rays in the RV Tauri subclass of post-AGB binaries. Finally, we summarize our conclusions in Section 3.7.

3.3 The U Monocerotis System

In this section we provide an observational overview of the U Mon system and review the physical properties that have been determined from previous studies. Table 3.1 summarizes the observed and derived physical properties that we use in our analysis.

Table 3.1: Observed and derived physical properties for the U Mon system used in our analysis.

Properties	Value	Reference
Spectral type	K0Ibpv	1
[Fe/H]	-0.8	2
[C/O]	0.8	2
T_{eff}	5000 K	2
Distance	1111^{+137}_{-102} pc	3[a]
Radius	$100^{+18.9}_{-13.2}$ $R_\odot$	3
Luminosity	5480^{+1764}_{-882} $L_\odot$	3
$Mass_{Post\text{-}AGB}$	$2.07^{+1.4}_{-0.9}$ $M_\odot$	3[b]
Pulsation formal period	91.48 days	4
RVb long-term period	2451 days	4
Binary		
Inclination	75°	5
Orbital period	2451 days	(fixed) 6
e	0.31 ± 0.04	6
T_0	2452203 ± 17 days	6
ω	$95^\circ \pm 7^\circ$	6
K_1	13.5 ± 0.7 km s^{-1}	6
Mass function	0.54 ± 0.12 $M_\odot$	6
$Mass_{Companion}$	$2.22^{+1.0}_{-0.75}$ $M_\odot$	6
Semimajor axis	$5.78^{+2.7}_{-1.4}$ au	6
Disk		
Diameter	$\lesssim 550$ au	6
Dust mass	$\sim 4 \times 10^{-4}$ $M_\odot$	6
Inner-disk edge radius	$\sim$ 4.5–9.0 au	6

References. (1) He et al. (2014); (2) Giridhar et al. (2000); (3) Bódi & Kiss (2019); (4) Kiss & Bódi (2017); (5) Oomen et al. (2018); (6) this study.

[a] Based on *Gaia* measurements. However, see note in text (Section 3.3.2) regarding the *Gaia* parallax accuracy and uncertainty.

[b] Average of the values from the Groenewegen & Jurkovic (2017) period–luminosity–mass relationships adopted in Bódi & Kiss (2019).

3.3.1 U Mon as an RV Tauri Variable of RVb Type

U Mon, a yellow supergiant variable (K0Ibpv; He et al., 2014), is located at a distance of 1111^{+137}_{-102} pc (Bódi & Kiss, 2019). It is the second-brightest RV Tauri variable (after R Sct) with a magnitude range of 5.45–7.67 in V (Watson et al., 2006), mean color index $B-V = 1.05$ mag at RVb brightness maximum, 1.11 mag at RVb minimum (Pollard et al., 1996), and a metallicity of [Fe/H] $= -0.8$ (Giridhar et al., 2000). Its formal pulsation period (deep + shallow minima cycle) is 91.48 days and its fundamental period is 45.74 days. U Mon also exhibits a long-term periodic modulation in mean brightness (RVb phenomenon) with a period of $\sim$ 2451 days (Kiss & Bódi, 2017), where the large-amplitude difference in mean brightness is $\sim$ 3 mag.

3.3.2 U Mon as a Binary Star System

With BVRI photometry and high-resolution spectra, Pollard & Cottrell (1995) concluded that U Mon is an eccentric binary (e = 0.43) exhibiting a radial velocity amplitude of 30 km s^{-1} (full amplitude) and an orbital period of $\sim$ 2597 days, which is similar to its photometric RVb period, as found in other RVb systems (Manick et al., 2017).

Oomen et al. (2018) recently updated the orbital properties of the U Mon binary system using data from the HERMES spectrograph on the 1.2 m Mercator telescope. They found an orbital period of 2549 ± 143 days. By assuming a typical post-AGB mass for the primary of 0.6 $M_\odot$ and an inclination of 75°, they estimated a projected semi-major axis of 3.38 ± 0.31 au, a mass function of 0.79 ± 0.18 $M_\odot$, and hence a minimum mass of 1.64 $M_\odot$ for the companion. However, most recently Bódi & Kiss (2019) used *Gaia* (DR2; Gaia Collaboration et al., 2018) data and two different period–luminosity–mass–temperature–metallicity relations derived by Groenewegen & Jurkovic (2017) (based on hydrodynamical atmosphere modeling of fundamental-mode pulsators from Bono et al. (2000); Marconi et al. (2015)), to empirically infer the mass of the post-AGB star in U Mon to be between 2.00 and 2.13 $M_\odot$. For our analysis we adopt the mean of these last two values (Section 3.5.2).

We note that the *Gaia* distance is likely biased by the orbital movement of the binary. The renormalized unit weight error (RUWE) for U Mon (RUWE = 2.4) indicates a poor single-star solution. High RUWE can be caused by a variety of factors, including resolved components in U Mon (see Belokurov et al., 2020). The astrometric excess noise (ε_{Gaia}) for U Mon in the DR2 catalog is 0.40 mas. This parameter is the excess uncertainty that must be added in quadrature to the formal uncertainties to obtain a statistically acceptable astrometric solution in the DR2 pipeline (Lindegren et al., 2012). Gandhi et al. (2020) considered using ε_{Gaia} as a proxy for the expected astrometric orbital wobble (ω) to help identify potential X-ray binaries. Given that the *Gaia* DR2 observations[2] occurred over only $\sim 25\%$ of the orbit of the U Mon system, the maximum expected orbital wobble for our orbit solution for U Mon at a distance of 1.1 kpc is ~ 0.3 mas, which is comparable to the reported ε_{Gaia} value, suggesting that the excess uncertainty could be mostly due to orbital motion. Indeed, the newly updated *Gaia* Early Data Release 3 parallax[3] of 1.28 ± 0.12 mas differs from the *Gaia* DR2 parallax by 0.36 mas, again very similar to ε_{Gaia}. Therefore, if we adopt ε_{Gaia} as the uncertainty in the parallax measurement, then the distance to U Mon ranges between $\sim$ 770 pc and $\sim$ 2 kpc. However, using the same period-luminosity-mass relations by Groenewegen & Jurkovic (2017) as were used originally by Bódi & Kiss (2019), we find that the stellar and orbital quantities in Table 3.1 do not change significantly relative to the already-quoted uncertainties. Therefore, we adopt the nominal distance of 1.1 kpc as in Bódi & Kiss (2019).

3.3.3 The U Mon Circumbinary Disk

As with many other RV Tauri variables in the literature, the U Mon binary star system is surrounded by a CBD. Bujarrabal et al. (2013) estimated the size of the U Mon CBD to be ~ 300 au using observations at the IRAM 30 m telescope in 2012–2013. Though they did not detect the Keplerian rotation of the CBD, they derived an upper limit for the molecular gas mass ($< 9 \times 10^{-4}$ $M_\odot$) from their ^{13}CO J=1$-$0 data.

[2] Section 1.3.1 Time coverage: https://gea.esac.esa.int/archive/documentation/GDR2/

[3] *Gaia* EDR3 was released on 2020 December 01.

In addition, Kluska et al. (2019) were able to reproduce their recent Very Long Baseline Interferometer (VLTI)/PIONIER near-IR (H-band) observations for U Mon by using their most complex model that includes a binary and inner ring. They suggested an an inner-disk diameter of ~ 5.9 AU.

3.3.4 Magnetic Activity in U Mon

Sabin et al. (2015) were the first to find magnetic fields at the surface of U Mon. The Stokes Q and U profiles were observed at RVb phase ~ 0.63 and the Stokes V profile at phase ~ 0.84 in Figure 3.6, respectively. They analyzed high-resolution spectropolarimetric ESPaDOnS (CFHT) data and found a clear Zeeman signature in the Stokes V profile. They measured a longitudinal magnetic field (i.e., in the line of sight) of 10.2 ± 1.7 G in the photosphere of U Mon. Although the sample is poor, this is to date the strongest surface field directly detected for a post-AGB star. The Stokes Q and U profiles indicated the presence of shocks, and the authors suggested the possible amplification of the magnetic field due to the atmosphere dynamics.

3.4 Data

3.4.1 Radial Velocity Observations

We adopted radial velocity observations of U Mon, corrected for the effects of surface pulsations, reported by Oomen et al. (2018, available on VizieR). Most photometric RVb periods of RV Tauri variables are similar to the orbital periods of their binaries (Manick et al., 2017). To calculate a new orbital solution for the binary in U Mon, we fixed the orbital period at 2451 days (U Mon's photometric RVb period; Bódi & Kiss, 2019), and we refit the data with a single-lined spectroscopic, Keplerian binary orbit model using `PHOEBE` (Prša et al., 2016). The resulting fit is shown in Figure 3.1, and the fit parameters are summarized in Table 3.1. We discuss our findings in Section 3.5.2.

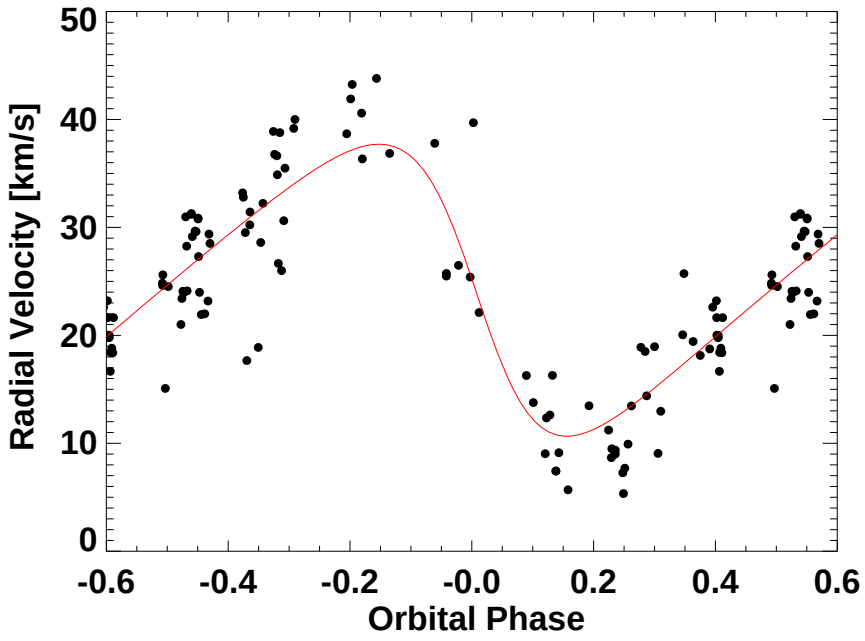

Figure 3.1: Single-lined orbit solution for U Mon as fit to the radial velocity observations of Oomen et al. (2018).

3.4.2 Light-curve Observations

We use two sources of long-term photometric monitoring of U Mon in order to explore secular changes in the U Mon light curve on timescales of decades or longer. The full light-curve data set is represented in Figure 3.2.

3.4.2.1 AAVSO

The American Association of Variable Star Observers (AAVSO) is a global network of amateur and professional astronomers dedicated to monitoring variable stars. The earliest observation of U Mon in the AAVSO archive was made by Ernest E. Markwick on 1888 December 25 (JD 2,410,997.0), and after a few observations there followed a 49 yr gap between 1896 and 1945. More regular monitoring began in the mid-1940s and continues to the present day. We downloaded all (including "discrepant"-flagged) Mag$_V$ data from the AAVSO database up to 2020 May 26. We chose to keep discrepant data since we are not focused here on the pulsation variability. We also wanted to make sure we had the data between 1888 and 1896 (which are all marked discrepant)

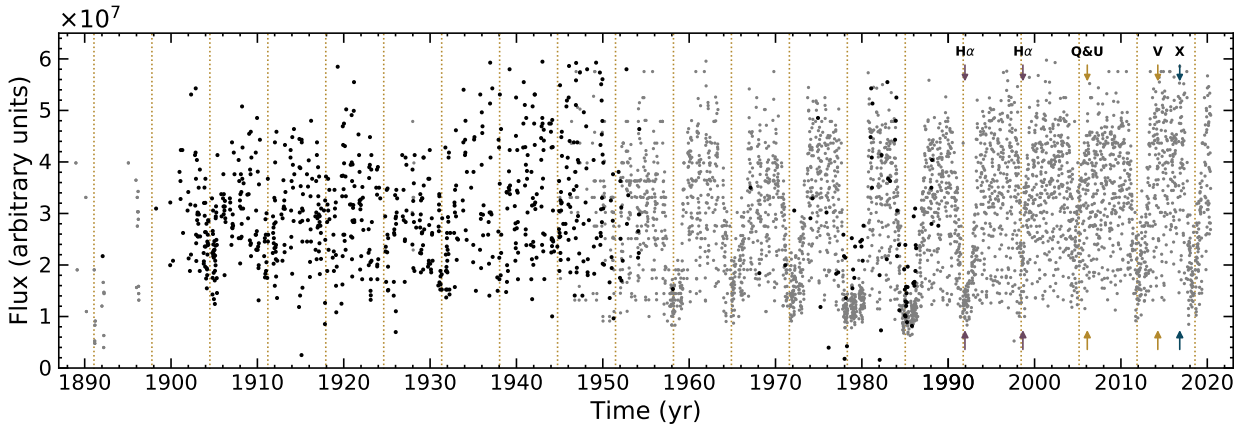

Figure 3.2: Final combined AAVSO (gray points) and DASCH (black points) light curve of U Mon, binned by 5 days. Both data sets overlap in time between 1945 and 1954, and during two long-term RVb cycles between 1974 and 1988. The scatter is due to the short-term pulsation variability. The times of apastron passage are represented by golden vertical dotted lines; the apastron times match with the RVb minima throughout the entire light curve (see Section 3.5.2). The arrows represent the observation times of the enhanced Hα (purple); the Stokes Q, U, and V profiles (gold); and X-rays (teal).

because they capture a long-term RVb cycle; these data are nonetheless useful for our purposes and fill a gap in time that is otherwise unavailable. We only excluded 36 Mag_V data points tagged as upper limits.

3.4.2.2 DASCH

The Digital Access to a Sky Century at Harvard (DASCH) survey is an ongoing effort to digitize about 0.5 million photographic plates covering the northern and southern sky from 1880 to 1985 (Grindlay et al., 2009).

Data for U Mon were released in the DASCH Data Release 6 (DR6). We downloaded the light curve of U Mon from the DASCH Light Curve Access pipeline website[4] using the default search radius of $5''$. Since the majority of the Harvard plates are close to Johnson B, we chose the data from the APASS B photometric calibration catalog, which yields the most accurate photometry (Tang et al., 2013).

The DASCH (APASS B-band catalog) light curve of U Mon (ID: T540046991) contained 3824

[4] http://dasch.rc.fas.harvard.edu/lightcurve.php

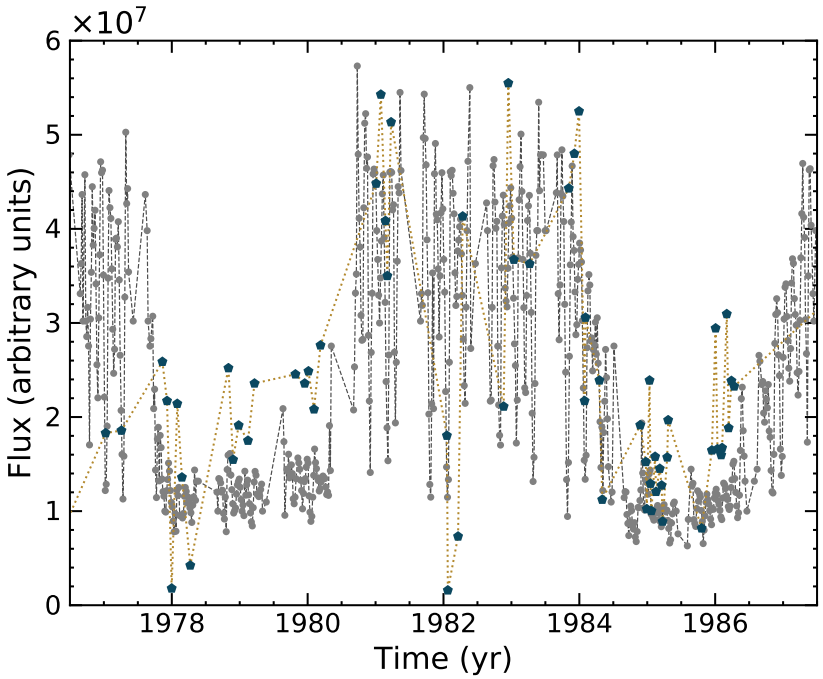

Figure 3.3: Two long-term RVb minima where the DASCH (teal pentagons) and AAVSO data (gray points) overlap the most in time. The grey dashed line on the AAVSO points (yellow dotted line for DASCH), though affected by the 5-day binning of the data, mainly highlights the pulsation variation of U Mon. Pulsation amplitudes during the RVb maxima may extend to as low as the mean magnitude at RVb minima, while the pulsations during RVb minima are always smaller in amplitude, showing the effect of disk obscuration of the pulsating post-AGB.

magnitude data points from approximately 3436 plates at the time of download. The light curve has a mean magnitude of 8.77 in B and a baseline going back to 1888 January 25 (JD 2410661.7) with occasional gaps, the largest one being the "Menzel" gap in the 1950s and 1960s, when the plate-making operation was halted by the Harvard Observatory director at the time owing to financial concerns. We excluded DASCH data points that had estimated errors of the locally corrected magnitude measurement (`magcal_local_rms`) values greater than 0.6 mag (which included `magcal_local_rms` values set to 99.0; these are tagged magnitudes from images dimmer than the limiting value of the image). We also excluded magnitude-dependent corrected magnitude (`magcal_magdep`) values brighter than 2.0 and dimmer than 11.0 (which were well away from the mean magnitude of the overall light curve).

3.4.2.3 Combining AAVSO and DASCH Light-curve Data

To analyze the AAVSO and DASCH data sets together, we converted the light curves to flux units using arbitrary zero-points (ZPs). For AAVSO we adopted ZP = 25 (Kiss & Bódi, 2017). Because the DASCH effective bandpass is different from the AAVSO Mag_V bandpass, we experimented with ZP values for DASCH to empirically determine a scaling factor and ensure a proper match of the AAVSO and DASCH data during two RVb cycle amplitudes (between 1974 October and 1988 August), where the AAVSO and DASCH data sets overlap to the greatest degree in time. We adopted ZP = 27.5 for DASCH as the best fit but found that we also had to scale the DASCH fluxes by a factor of 1.21 and then subtract 1.1×10^7 flux units to match the two overlapping RVb cycles (see Figure 3.3). After we converted to arbitrary flux units, we made another cut to exclude data above $\sim 6 \times 10^7$ flux units and ≤ 0.

The final combined AAVSO+DASCH light curve is shown in Figure 3.2. It is an impressive data set, spanning the period from $\sim$ 1890 to $\sim$ 2020. The light curve is binned by 5 days to average out errors of individual observations and to reduce phase smearing due to the binning (Kiss & Bódi, 2017). What seems to be leftover scatter is actually due to pulsations of different amplitudes, as well as large gaps in the data (see, e.g., Figure 3.3). Several features are present in the secular changes of the light curve on timescales of decades, and we discuss this in Section 3.5.1.

3.4.3 SMA Observations

The SMA is an interferometer, composed of eight 6 m dishes, that observed U Mon on three occasions. On 2018 February 1, we observed the source in the subcompact array configuration with projected baselines of 7–49 m and covered two frequency ranges at 223.6–231.6 GHz and 239.6–247.5 GHz. On 2018 October 2, observations were made at higher frequencies, from 328.8 to 360.8 GHz, and at longer baselines of 6–70 m. On 2019 March 15, we finally observed U Mon in the very extended SMA configuration (VEX) with baselines from 32 to 514 m. The covered frequency ranges were 209.1–212.8 GHz, 214.9–216.7 GHz, 225.1–226.9 GHz, 229.2–238.8 GHz,

332.8–340.8 GHz, and 348.8–356.8 GHz. The spectral coverage in the VEX observations is smaller than on the earlier dates owing to a nonfunctional quadrant of the SMA correlator SWARM (Primiani et al., 2016) at that time. All eight SMA antennas were used for our first two observing runs except for observations in VEX at low frequencies for which only six antennas had properly functioning receivers.

Because the target was observed mainly as a filler project,[5] the final *uv* coverage is suboptimal, in particular, very inhomogeneous at higher frequencies. The complex antenna gains were calibrated in all observing runs by observations of quasars J0730–116 and J0725–009. The bandpass was calibrated using long integrations of quasars 3C 279 and 3C 84. An absolute flux scale was established by observations of Uranus (on February 1), Neptune (on October 2), and Callisto (in 2019). The calibration was performed in `MIR` software using standard procedures[6]. Further data processing, including imaging, was performed in `CASA` (McMullin et al., 2007).

Calibrated visibilities measured in the different array configurations were combined within the two atmospheric windows near 345 GHz ($\sim$ 0.8 mm) and 230 GHz (1.3 mm) and their weights rescaled to the actual noise levels. This resulted in continuum sensitivities of $\sigma_{345} =$ 4.0 mJy beam^{-1} and $\sigma_{230} = 0.89$ mJy beam^{-1} at beam sizes of $4.0'' \times 2.4''$ and $0.9'' \times 0.6''$, respectively. These beam sizes correspond to natural weighting of visibilities. In both bands the continuum source was readily detected at flux levels listed in Table 3.2; see also Figure 3.4. No spectral lines were detected with an rms noise level of 39.3 mJy beam^{-1} near the frequency of the CO J=2–1 line and at a 3.9 km s^{-1} spectral binning, which is consistent with the nondetection reported by Bujarrabal et al. (2013). We discuss U Mon's submillimeter emission in Section 3.5.5.

3.4.4 XMM-Newton Observations

U Mon was observed by the X-ray Multiple Mirror (XMM-Newton) observatory on 2016 October 23 for 58.3 ks (RVb phase $\sim$ 0.23 in Figure 3.6). The XMM-Newton observations include

[5] http://sma1.sma.hawaii.edu/call_filler.html
[6] http://www.cfa.harvard.edu/~cqi/mircook.html

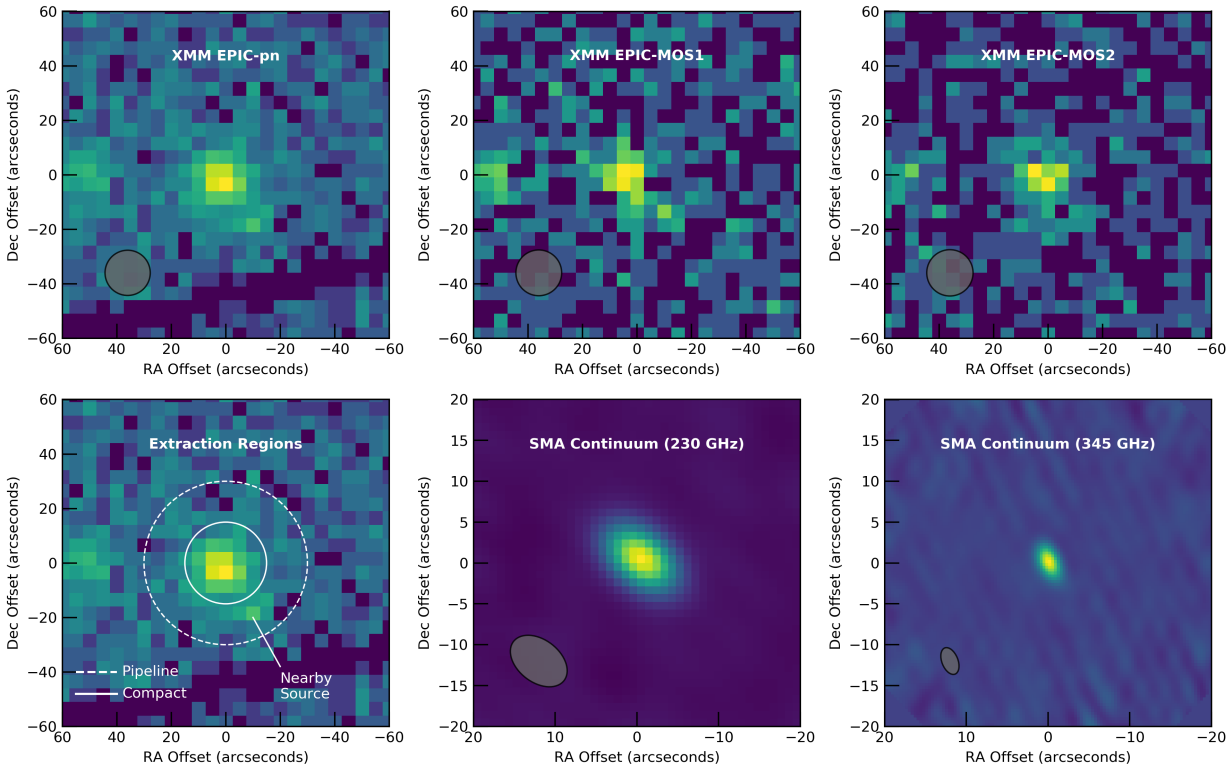

Figure 3.4: Top panels: XMM EPIC-pn, EPIC-MOS1, and EPIC-MOS2 images with a clear detection of X-rays for U Mon. Bottom left panel: The EPIC-pn image annotated with the pipeline extraction vs. our compact extraction region excluding the nearby source near U Mon. Bottom middle and right panels: U Mon's SMA continuum images at 230 GHz (1.3 mm) and 345 GHz (870 μm), respectively. The respective beams are included in the lower left corners in dark gray.

15 imaging exposures: three X-ray images on the EPIC-pn (55.3 ks), EPIC-MOS1 (57.0 ks), and EPIC-MOS2 (56.9 ks) detectors, and 12 exposures (each $\sim$ 2.2–4.4 ks) with the Optical Monitor (OM) using the UVW1, UVM2, and UVW2 filters. Representative images are shown in Figure 3.4. U Mon is detected in all imaging exposures. Additionally, there are two grating dispersed exposures in X-ray emission on the RGS1/2 (57.2 ks), but the dispersed spectrum is not detected. The large source region used to generate the pipeline products leads to confusion and blending with a nearby source (see bottom left panel in Figure 3.4). We re-extracted the X-ray spectra and light curves using a smaller source region with a radius of 15$''$ and a source-free background region near the source. The extracted spectral products were corrected for the reduced extraction region by accounting for the encircled energy fraction in the response files.

3.4.5 Spectral Energy Distribution Data

To construct U Mon's SED, we downloaded available archival photometric data from VizieR. We did not take into account the phase of observations (i.e. either at maximum/minimum pulsation or long-term RVb brightness). We included Herschel-PACS/SPIRE measurements (downloaded from the ESA Herschel Science Archive[7]; PI: C. Gielen), the 850 μm flux value reported by de Ruyter et al. (2005) taken with the Submillimetre Common-User Bolometer Array (SCUBA) at the James Clerk Maxwell Telescope (JCMT), and finally millimeter fluxes from Sahai et al. (2011) taken at the Combined Array for Research in Millimeter-wave Astronomy (CARMA).

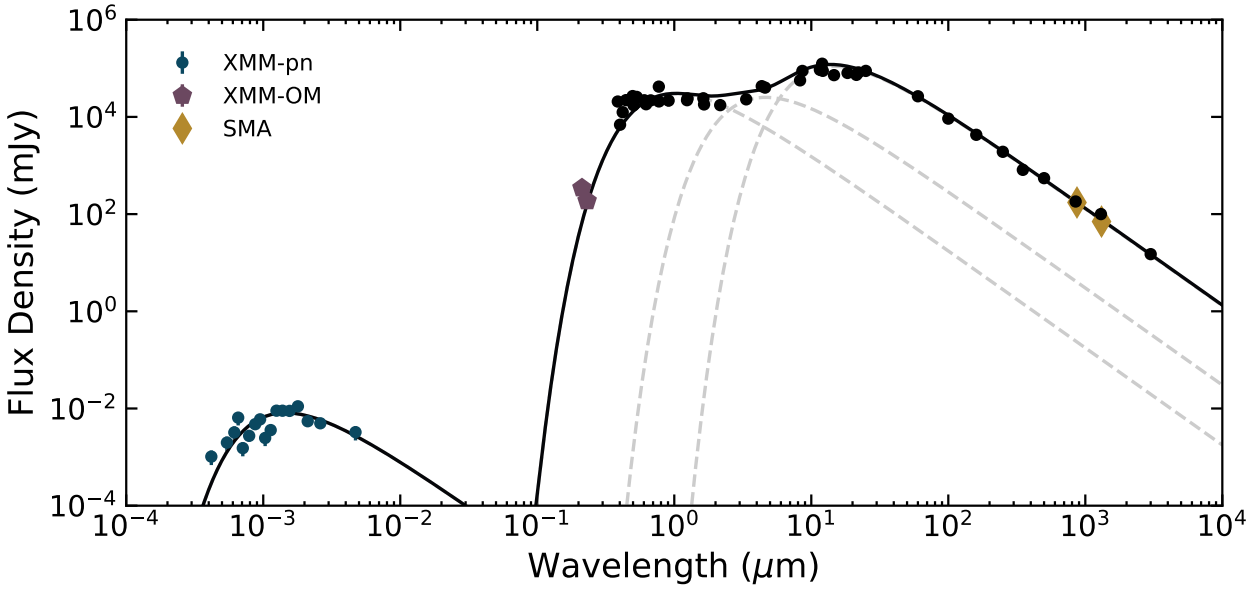

Figure 3.5: SED for U Mon. Representative archival data (black points) were collected from VizieR and the Herschel archives, as well as the 850 μm measurement from de Ruyter et al. (2005) and the 1.3 and 3 mm measurements from Sahai et al. (2011). We present the new XMM-pn spectrum in teal points, the XMM-OM data in pentagons, and the SMA data in diamonds. The scatter in the archival data is probably due to intrinsic (pulsation or RVb) variability of U Mon at the time of observation. Note: error bars are smaller than the symbols.

The new observations we contribute in this paper are submillimeter and UV/X-ray from the SMA and XMM-Newton, respectively. Our SMA 870 μm and 1.3 mm values are similar to those reported by de Ruyter et al. (2005) and Sahai et al. (2011), respectively. The XMM-OM magnitudes for U Mon were converted to flux density (Jy) using the ZPs from Mason et al. (2001). To

[7] http://archives.esac.esa.int/hsa/whsa/

Table 3.2: New flux measurements for U Mon.

Wavelength (μm)	Flux (mJy)	Date	System
0.212	23.27 ± 0.038	2016 Oct	XMM-OM:UVM2
0.231	16.30 ± 0.030	2016 Oct	XMM-OM:UVW2
869.4	173.3 ± 6.5	2018 Feb, Oct; 2019 Mar[a]	SMA
1313	70.2 ± 8.5	2018 Feb, Oct; 2019 Mar[a]	SMA

[a]Combined observations.

represent the XMM EPIC-pn spectrum, we unfolded the instrumental response from the spectral data assuming the best-fit model determined using the X-ray Spectral Fitting Package (XSPEC[8]; Arnaud, 1996), dereddened the spectral data (see Section 3.5.3), and then converted from photon flux densities to Jy.

Figure 3.5 shows the SED for U Mon, and Table 3.2 lists our new flux measurements. In Section 3.5.3 we discuss the blackbody models we used on the SED.

3.5 Results

3.5.1 Secular Variations of the U Mon Light Curve over the Past Century

The long-term RVb cycles of the U Mon light curve are more salient in the AAVSO data, and we can estimate the duration of the maxima more easily than the minima. Overall, the RVb phenomenon in U Mon changes significantly from cycle to cycle. The RVb maxima range between $\sim$ 3.3 and 4.8 yr, whereas the RVb minima differ even more, from several months to the longest minimum lasting $\sim$ 2.5 yr (e.g., between $\sim$ 1977.8 and 1980.5; see Figure 3.3).

In Figure 3.6 we explore longer-term secular changes in the light curve, enabled by unprecedented coverage spanning $\sim$ 130 yr. We binned both data sets by U Mon's fundamental pulsation period (45.74 days) to focus on the RVb behavior. We plot the DASCH data in black, the AAVSO data in gray, and the DASCH data that distinctly overlap the two RVb cycles during 1975–1988 as

[8] http://heasarc.gsfc.nasa.gov/xanadu/xspec/

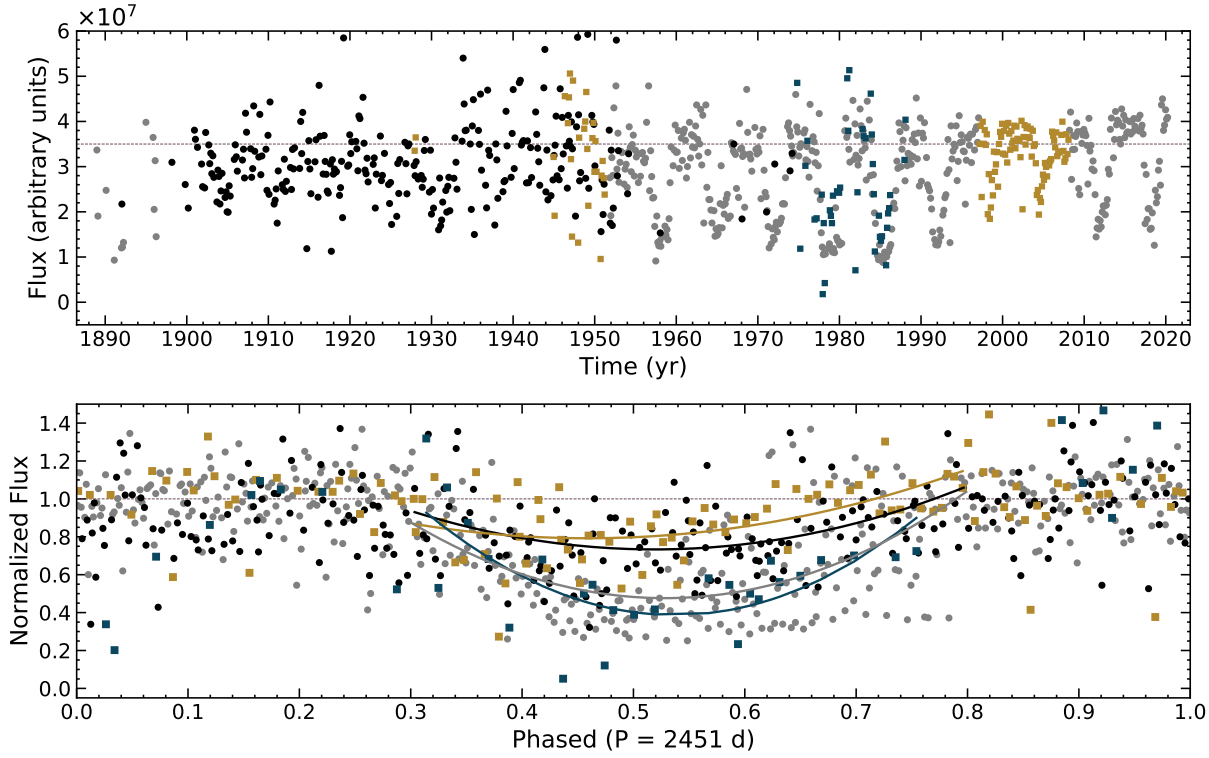

Figure 3.6: Analysis of secular variations in the U Mon light-curve data. Top: light curve binned by the fundamental period 45.74 days. The black points are DASCH data, the gray points are AAVSO data, the DASCH data overlapping two distinct RVb cycles are shown as teal squares, and the golden squares define AAVSO data sporadically overlapping DASCH data before 1951 and data corresponding to what might be times of partially obscured minima ($\sim$ 1997–2008). The dashed line is the mean flux at RVb maximum (3.5×10^7 flux units). Bottom: light curve phase-folded on the 2451-day RVb period of the system with flux normalized at unity at the base level (dashed line is the same as the top panel). See Section 3.5.1 for a discussion of the curves.

teal squares. We also define golden squares that are AAVSO data sporadically overlapping with DASCH data before 1951, and AAVSO data corresponding to what might be times of partially obscured RVb minima ($\sim$ 1997–2008). The top panel is the binned light curve in time, the bottom panel is the binned light curve phased by the RVb period of 2451 days, and the flux is normalized to be unity at the base level. We fit parabolas to the data at phases of 0.5 ± 0.3, to get a cleaner visual sense of how the RVb minima compare for the various subsets.

We find that the AAVSO data (gray points) and the DASCH overlap data (teal squares) have nearly identical RVb minima. Similarly, we see that the older DASCH data (black points) and the

golden-square AAVSO data have nearly identical RVb minima, and the latter minima are about a factor of 2 less deep. In other words, it appears from the historical record that the RVb variations—which have come to be associated with a highly inclined disk shadowing the primary at certain orbital phases—have largely disappeared at least twice in the past, with a timescale of $\sim$ 75 yr, from the middle of the black points to the latest golden squares in Figure 3.6.

Another way to examine this is shown in Figure 3.7, in which the disappearance of the RVb variation, due to the large scatter in the data points, is more obvious for two RVb minima in 1938 and 1944 and then again in 1998 and 2005, with a timescale between them of $\sim$ 60.4 yr, which we note is nine times the RVb long period. To be clear, the RVb minima are short during these cycles ($\sim$ several months, as opposed to years), and they "disappear" relative to the large scatter/pulsation variations from the (particularly longer) maximum state at either side of RVb minima. We further discuss the interpretation of this phenomenon in Section 3.6.1.

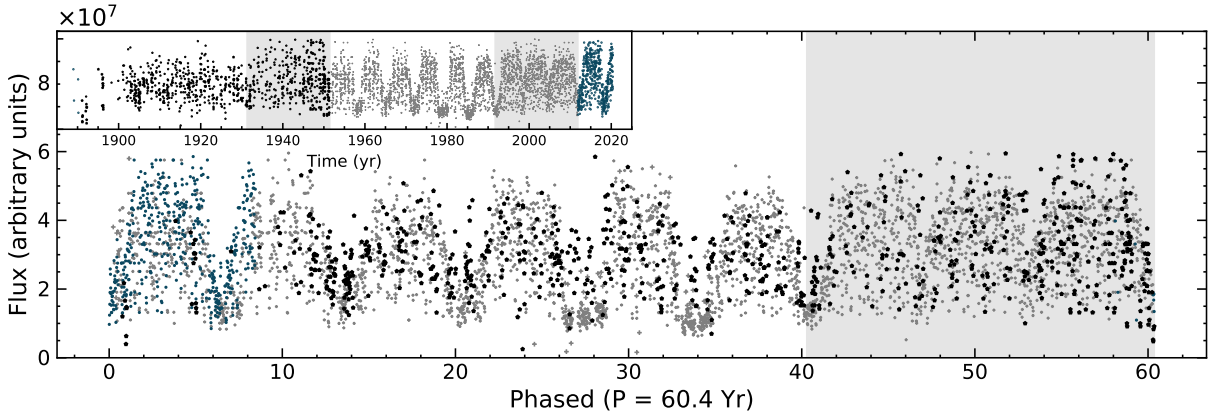

Figure 3.7: Light curve of U Mon phased at 60.4 yr (nine RVb cycles). The inset shows the full light curve divided in color distinguishing the two 60.4 yr cycles in the data (black points represent the first 60.4 yr cycle; gray points, second cycle). The start of a third cycle is shown as teal points. The RVb cycles highlighted in light grey include long ($\lesssim$ 4.5 yr) RVb maxima and short RVb minima (phase $\sim$ 47 yr and $\sim$ 53 yr) that have durations of only several months based on the AAVSO data.

3.5.2 Orbital Properties of the U Mon Binary Star System

From the orbit fit in Section 3.4.1, we obtained orbital parameters (listed in Table 3.1) that are within the errors of the values consistent with Oomen et al. (2018), including a new periastron time of $T_0 = 2452203 \pm 17$ days. Adding half (1225 days) of the fixed orbital period to the periastron time gives an apastron at JD = 2453428 days. Multiples of the orbital period with the apastron time give all apastron events (denoted as golden vertical dashed lines in Figure 3.2) that roughly align with the RVb minima throughout U Mon's entire DASCH+AAVSO light curve. Mass estimates for U Mon range from a fiducial post-AGB mass average of 0.6 $M_\odot$ (Gezer et al., 2015; Manick et al., 2017; Weidemann, 1990) to most recent values of 2.00 and 2.13 $M_\odot$ reported by Bódi & Kiss (2019). To estimate a value for the companion's mass (M_2), we used the average value from Bódi & Kiss (2019) for the mass of the post-AGB (M_1 = 2.07 $M_\odot$) in Equation 3.1 (the binary mass function for an eccentric orbit) and solved for M_2:

$$f(m) = \frac{PK_1^3}{2\pi G}(1-e^2)^{\frac{3}{2}} = \frac{M_2^3}{(M_1+M_2)^2}\sin^3 i. \tag{3.1}$$

Using the recalculated radial velocity curve, and keeping the orbital inclination maximum limit of 75° (Oomen et al., 2018), we find the mass for the companion to be $2.2^{+1.0}_{-0.75}$ $M_\odot$; this mass range corresponds to an F-type or A-type star on the main sequence. Then, by using Kepler's third law, we derived a value of $5.78^{+2.7}_{-1.4}$ au for the semi-major axis. These parameters are reported in Table 3.1.

3.5.3 Spectral Energy Distribution

We dereddened the flux data between 0.2 and 3.3 μm using functions contained in the `Astropy`-affiliated package `dust_extinction`, with the F19 Milky Way R(V) dependent extinction (Fitzpatrick et al., 2019) using the standard value Rv = 3.1 and total extinction: $E_{B\text{-}V}$ = 0.3 (de Ruyter et al., 2005).

We made use of the `astropy.modeling.blackbody` routine (Astropy Collaboration

et al., 2013) to depict scaled blackbody components on the SED (these are not fitted). We include two blackbody components with temperatures of 5000 and 1100 K to represent the stellar atmosphere (Bódi & Kiss, 2019) and the inner-disk edge (see Section 3.5.4), respectively. We also include a modified blackbody (i.e., "graybody"; Casey, 2012) component with a mean temperature of 350 K to represent the dust in the extended disk. Finally, we added a 3.5 MK thermal blackbody for the X-ray spectrum.[9] Figure 3.5 shows the entire SED model as a black solid line, with the individual components depicted as light-gray dashed lines.

We integrated the 5000 K blackbody model (between ~ 0.2 and 2 μm), which gave a (dereddened) bolometric flux of $F_{bol} \approx 1.44 \times 10^{-7}$ erg s^{-1} cm^{-2}, corresponding to $L_\star \sim 5556$ $L_\odot$ and yielding a physical radius of $R_\star \sim 100$ $R_\odot$.

We tested how an additional blackbody component with the properties of the putative A-type companion star (9800 K and 55 $L_\odot$) would influence our SED model and found that such a companion would remain undetectable in the SED (even at RVb minimum) owing to the brightness of the post-AGB component (see Section 3.6.3).

Assuming that the dust is optically thin at $\lambda = 870$ μm, we used the following expression (e.g. Hildebrand, 1983) to estimate the mass of the dust in the disk:

$$M_d = \frac{F_\lambda D^2}{\kappa_\lambda B_\lambda(T_d)}, \tag{3.2}$$

where $B_\lambda(T_d)$ is the blackbody intensity at the Rayleigh-Jeans limit in the form of $\frac{2k_{SB}T}{\lambda^2}$. Using a mean dust temperature T_d = 350 K, our observed SMA flux F_{870} = 173.3 mJy, D = 1.1 kpc (Bódi & Kiss, 2019), and a dust opacity of $\kappa_\lambda = 2.0$ cm^{2}g^{-1} at 870 μm (Ladjal et al., 2010), we estimate a total dust mass of $M_d \sim 4 \times 10^{-4}$ $M_\odot$. For a typically assumed gas-to-dust ratio of 200 (e.g. Groenewegen et al., 2007, 2009) the total dust mass suggests a gas mass of $\sim 8 \times 10^{-2}$ $M_\odot$; however, this gas mass is much larger than the constraint of the molecular mass estimated by Bujarrabal et al. (2013). The lack of molecular gas may be related to high-energy radiation that

[9] The blackbody model is only shown for display purposes, the unfolded spectrum has a strong dependence on the best-fit 10 MK plasma model, and a blackbody model does not provide a suitable fit to the observed X-ray spectrum.

has been dissociating molecules present in the system that would support the larger distance to U Mon. Since the primary star is not hot enough, the presence of a hotter companion or interstellar UV field could photodissociate molecules in the inner and outer disk regions (Bujarrabal et al., 2013).

3.5.4 Properties of the Circumbinary Disk's Inner Edge

The radius of the near-IR emission, where dust can be sublimated by stellar radiation, can also set the physical radius of the inner boundary of the disk (Dullemond et al., 2001; Monnier & Millan-Gabet, 2002; Hillen et al., 2017; Kluska et al., 2019; Lazareff et al., 2017). Using the following luminosity–radius relation (e.g. Lazareff et al., 2017), we estimated the inner-rim radius (R_{rim}) of the CBD for U Mon:

$$R_{\rm rim} = \frac{1}{2}\left(\frac{C_{\rm bw}}{\varepsilon}\right)^{1/2}\left(\frac{L_\star}{4\pi\,\sigma\,T_{\rm sub}^4}\right)^{1/2}, \tag{3.3}$$

where we adopted $L_\star$ = 5480 $L_\odot$ (Bódi & Kiss, 2019) as the stellar luminosity. C_{bw} is the back-warming coefficient of the inner-disk edge that ranges between $\sim$ 1 and 4, where $C_{bw} = 1$ provides a lower limit on R_{rim} and $C_{bw} = 4$ provides an upper limit on R_{rim} (Monnier et al., 2005; Kama et al., 2009). The cooling efficiency of the dust grains, defined by $\varepsilon = \kappa(T_{dust})/\kappa(T_\star)$, is a ratio between the Planck mean opacity (κ) of the dust species at its own temperatures and that at the stellar temperature, where $\varepsilon \leq 1$, and generally increases with grain size (Kama et al., 2009). For the dust in the CBD, we assume $\varepsilon \sim 1$. Typically, for oxygen-rich dust species ([C/O] of 0.8 for U Mon), the sublimation temperature (T_{sub}) is $\sim$ 1100 K (Bladh et al., 2013). We note that Kluska et al. (2019) suggest a higher inner-dust temperature ($\sim$ 2600 K) for U Mon but only reach a moderate fit with their most complex model, whereas most of their sample of post-AGB binaries have near-IR circumstellar emission sublimation temperatures lower than 1200 K. Finally, the range between $C_{bw} = 1$ and $C_{bw} = 4$ gives an R_{rim} between $\sim$ 4.5 and 9.0 au, respectively.

3.5.5 Submillimeter Emission from U Mon

The SMA observations in the combined array configurations and uniform weighting of visibilities resulted in continuum maps with synthesized beam sizes of $0.69'' \times 0.37''$ at 1.3 mm and $0.39'' \times 0.24''$ at 0.87 mm, respectively. Simple fits of elliptical Gaussians to the map at 0.87 mm give a source size of $(0.89'' \pm 0.34'') \times (0.20'' \pm 0.39'')$ and an orientation of the longer axis at a position angle (P.A.) of $55^\circ \pm 24^\circ$. The map at 1.3 mm indicates that the source size is much smaller than the beam, i.e. with FWHM $\lesssim 0.55''$. To better constrain the size and make best use of the data, we directly tried to fit a model source to the calibrated visibilities. Best solutions for an elliptical Gaussian and an elliptical uniform disk were found in a CASA task `uvmodelfit` and are presented in Table 3.3.

Table 3.3: Results of model fits to visibilities of U Mon measured with the SMA.

Band	Model	Major (mas)	Minor/Major	P.A. (deg)
1.3 mm	Gaussian	299 ± 11	0.73 ± 0.04	83 ± 5
1.3 mm	Unif. disk	483 ± 24	0.76 ± 0.05	84 ± 8
0.8 mm	Gaussian	244 ± 6	0.86 ± 0.03	55 ± 7
0.8 mm	Unif. disk	482 ± 64	1.0 ± 0.2	–

For Gaussian models, FWHM is given as the major-axis size.

The model fits indicate a nearly circular source with a Gaussian FWHM smaller than about 500 mas, which corresponds to a disk diameter $\lesssim 550$ au at the nominal distance of 1.1 kpc. A denser *uv* coverage of observations at longer baselines would be necessary to better constrain the size of the submillimeter source.

The SMA fluxes are consistent with earlier observations in the nearby bands and represent the coolest component of U Mon's SED, which is consistent with a dusty source of T_d = 350 K (see Section 3.5.3).

3.5.6 X-Ray and UV Emission from U Mon

This is the first X-ray detection of an RV Tauri variable by any X-ray telescope. The X-rays are consistent with the location of U Mon within the pointing uncertainties and the fairly broad point spread function of the XMM EPIC X-ray detectors (FWHM $\sim 12''$). There is an additional but fainter source near the position of U Mon with a separation of $\sim 20''$ (see Figure 3.4). Given the relative brightnesses of the two sources and the radius used to extract the X-ray products, contamination by the nearby source is minimal.

The spectra were modeled using an absorbed (`tbabs`; Wilms et al., 2000), optically thin plasma model with variable abundances (`vapec`; Smith et al., 2001; Foster et al., 2012). Model fitting was performed with `XSPEC` (Arnaud, 1996). No acceptable fit could be found with solar abundances, but adequate fits were found when Fe was allowed to vary. Given the limited energy resolution and moderately low count rate of the CCD spectrum, we could not obtain meaningful constraints on both the plasma properties (temperature and normalization) and the important elemental abundances in the energy range of the detected emission (C, N, O, Ne, Mg, and Fe). Instead, we fixed the Fe abundance to a previously reported value of [Fe/H] =-0.79 and C-to-O ratio to 0.8 (Giridhar et al., 2000). The O abundance was allowed to vary along with the overlying absorption, plasma temperature, and plasma model normalization. The best-fit parameters are presented in Table 3.4 along with the absorbed and intrinsic X-ray fluxes and source luminosity for a distance of 1.1 kpc (Bódi & Kiss, 2019). The best-fit spectral model is displayed with the X-ray spectra in Figure 3.8, and the unfolded spectrum is presented in the multiwavelength SED in Figure 3.5; confidence level contours are shown in Figure 3.9.

Our analysis of the X-ray observations suggests that the emission is consistent with an iron-deficient hot ($\sim$ 10 MK) plasma with moderate absorption. The absorption reported in Table 3.4 is consistent with extinction to U Mon ($E_{B-V} \sim$ 0.3 mag; de Ruyter et al., 2005). The X-ray light curve reveals no evidence of flaring activity at the 3σ level; however, the light curves required 10 ks temporal bins to net sufficient signal-to-noise ratio. Hence we cannot evaluate activity on shorter time-scales. We discuss the origin of the X-ray emission in further detail in Section 3.6.3.

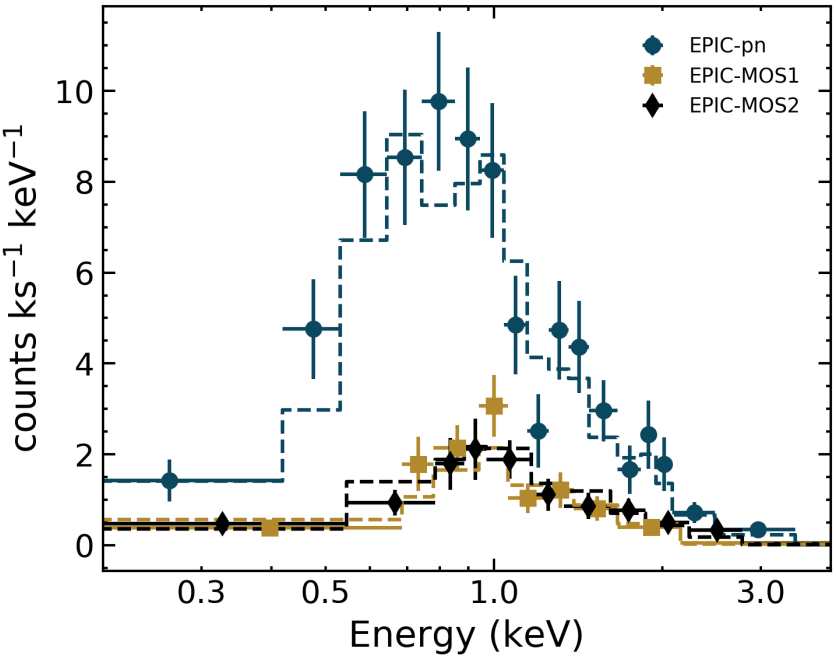

Figure 3.8: U Mon's X-ray spectra and best-fit spectral model (see Table 3.4).

Table 3.4: X-ray spectral fit results for U Mon.

Quantity	Value
$N_{\rm H}$ (10^{21}cm^2)	$1.2^{+0.6}_{-0.5}$
$T_{\rm X}$ (10^6 K)	12^{+1}_{-2}
Oxygen abundance[a]	$3.4^{+3.0}_{-1.6}$
Iron abundance	0.16
Model normalization (10^{-5})	$2.1^{+0.3}_{-0.3}$
$F_{\rm X,abs}$ [b] (10^{-14} erg cm^{-2} s^{-1})	$2.2^{+0.4}_{-0.4}$
$F_{\rm X,unabs}$ (10^{-14} erg cm^{-2} s^{-1})	$3.4^{+0.6}_{-0.6}$
EM (10^{53} cm^{-3})	3^{+1}_{-1}
$L_{\rm X}$ (10^{30} erg s^{-1})	5^{+1}_{-1}

[a]Abundances are number relative to solar values from Anders & Grevesse (1989). Iron abundance has been fixed to the [Fe/H] value of (Giridhar et al., 2000) after conversion to the number relative value.
[b]Model-derived fluxes have been corrected for the encircled energy fraction of the extraction region.

The XMM Optical Monitor performed numerous exposures in three UV filters: UVW1, UVM2, and UVW2 (with effective wavelength of 0.291, 0.231, and 0.212 μm, respectively). U Mon is detected in all three bands but saturated in UVW1. The UVM2 and UVW2 measurements are

included in the multiwavelength SED in Figure 3.5 and in Table 3.2. The UV light curves show variability consistent with Poisson noise. Given the short time frame for the UV observations, we are not very sensitive to variations or trends related to the pulsation period or the long-period variation.

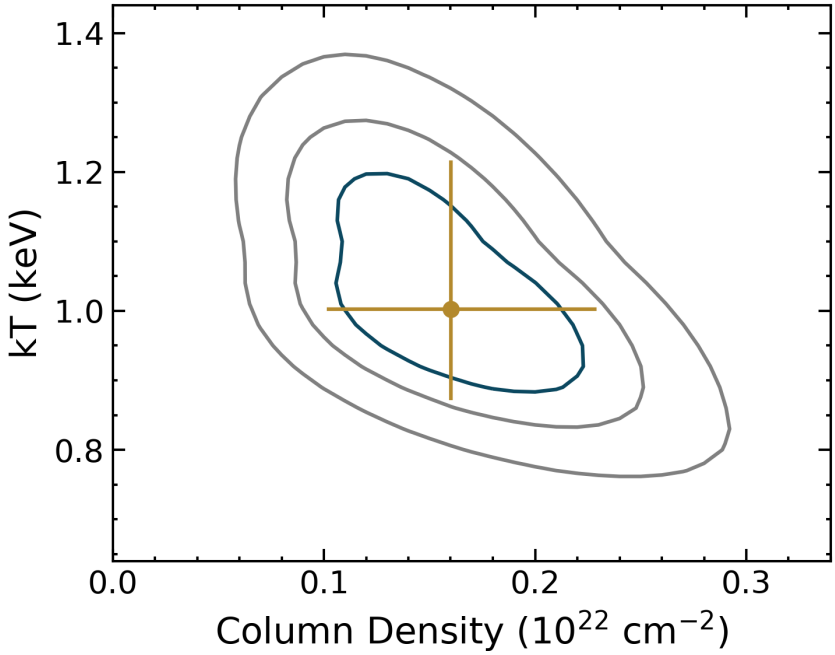

Figure 3.9: Best-fit confidence map for the plasma temperature (kT) and column density ($N_{\rm H}$) of the X-ray spectral fit. The best-fit solution is depicted with a 98% confidence range, and 68%, 90%, and 98% confidence levels are depicted.

3.6 Discussion

3.6.1 A 60 yr Trend in the Light Curve

U Mon's RVb behavior has been observed since before the 1900s, giving a window into the behavior of the CBD. Even with the lack of uniform monitoring in combination with various physical processes present (e.g., pulsations), an even slower trend in the light curve is still detected in the AAVSO+DASCH light curve.

In particular, three RVb cycles between 1931 and 1951 have significantly more scatter, com-

pared to the overall light curve. They resemble three cycles between 1991 and 2011 (see Figure 3.7). The disk-shadowing interpretation can be a possible explanation for the disappearance of the long-term variation or the lack thereof. This phenomenon can represent times when the RVb minima have become shallower and shorter, perhaps indicating some kind of precession of the binary or of disk-structure inhomogeneity at the inner-disk edge caused by binary–disk interaction (e.g. Kluska et al., 2018; Oomen et al., 2020).

Furthermore, the light curve hints of a different feature of two even deeper RVb minima that occur around 1925 and more clearly around 1985 (phase $\sim$ 34 yr in Figure 3.7) with the same time separation of $\sim$ 60.4 yr. A warp or a dense feature at the inner edge of the disk orbiting around it would only take about 6 yr (2190 days), which is comparable to the orbital period. If a warp or dense feature is farther out in a Keplerian orbit, it would have to be at a distance of 25 au to block out more of the post-AGB so that the RVb minimum becomes deeper every 60.4 yr.

As more photometric monitoring and interferometric imaging become available for post-AGB binaries, the detection of CBD warps or features may give rise to future investigations on possible second-generation planet formation such as in studies around other evolved stars (e.g. Hardy et al., 2016; Homan et al., 2018).

3.6.2 Circumbinary Disk Interaction

Pollard & Cottrell (1995) and Pollard et al. (2006) found enhanced Hα emission in U Mon during the RVb minima. This phenomenon is reminiscent of one observed in other binary star systems with eccentric orbits within CBDs, in which matter is pulled from the inner edge of the disk and onto the stars at apastron (e.g., Artymowicz & Lubow, 1996; Basri et al., 1997). Based on the periastron time occurring at RVb maximum, we experiment with the idea that the relevant time to explain the interaction that produces Hα enhancement is not at periastron but rather the time when the two stars are farthest apart (apastron), which would be when the stars would presumably be most likely to interact with the inner edge of the CBD.

Based on our orbital fit for the binary, the argument of periastron ($\omega = 95^\circ \pm 7^\circ$) means that

the longest dimension of the ellipse is oriented parallel to our line of sight. In other words, when the two stars are farthest apart, they are also along our line of sight during apastron, which happens during RVb minima. This scenario requires that the post-AGB be mostly hidden by the CBD while the companion travels in the background at an elevated angle crossing our light of sight and possibly interacting with the inner edge of the CBD, causing the enhanced Hα emission observed by Pollard et al. (2006) during RVb minima. This is also shown from the radial velocities in Figure 3.1, which measure the motion of the post-AGB star. The orbital phase of zero is at periastron (which corresponds to RVb maximum).

The nature of the CBD–binary interaction is not yet clear in post-AGB binaries; however, processes such as photospheric chemical depletion show that it is crucial. Interestingly, U Mon's photosphere does not show signs of depletion (Giridhar et al., 2005; Gezer et al., 2015); this could be because depletion is mostly observed in stars hotter than 5000 K (Venn et al., 2014). It is also possible that the depletion process could be interrupted by wind Roche lobe overflow onto the companion (Mohamed & Podsiadlowski, 2007).

The recent study by Oomen et al. (2020) investigated a few disk–binary interaction mechanisms for post-AGB binaries with orbital periods of 100–2500 days and eccentricities $\gtrsim 0.3$. They concluded that disk–binary interactions are unlikely to pump the eccentricity to the observed values within the evolutionary timescales for the stars they sampled. U Mon is not very eccentric (e = 0.31); this may suggest a weak disk–binary interaction.

However, the Kluska et al. (2019) geometric image reconstruction model of U Mon's visibility profile resulted in a fit that displayed strong azimuthal modulation, showing that this system likely has a very complex inner-disk morphology. Additionally, they showed that U Mon has a relatively large mid-IR-to-near-IR size ratio. The authors note that it is possible that the model is not able to reproduce all the complexities, which could have an effect of on their derived size of the CBD's inner rim; thus, further observations will bring stronger constraints. Such complexities have been seen in some YSO CBD systems, which can be regarded as scaled-down versions of the CBDs around post-AGB binaries (e.g. Hillen et al., 2017). For example, in the CBD of the young binary

GW Ori, imaging observations by Kraus et al. (2020) find evidence for an inner ring and a large warp in the outer part of the disk. This phenomenon occurs when the outer disk is misaligned with the orbital plane, so it wraps and breaks into precessing rings, which may provide a mechanism for planet formation.

Bollen et al. (2019) provide a detailed investigation on the possibilities for jets in explaining the Hα emission feature observed in post-AGB systems. In their model, the Hα feature is superimposed on the photospheric absorption from the post-AGB star and is present throughout the entire orbit. To establish whether such a jet scenario may apply to U Mon as well would require phase-resolved, high-resolution spectroscopy of the Hα feature.

If, instead, there is a stream outflow coming off the CBD onto the companion, always traveling around the companion and opposite of the post-AGB primary, the Hα enhancement would have a timescale near the binary orbital period. The stream of material would be at a focus point where it would be enhanced around apastron because that would be the shortest distance the CBD material would flow onto the companion. The stability for the shortest orbit of material around a binary should be at least $\sim$ 3–4 times the binary separation (Holman & Wiegert, 1999). However, it is possible that the inner edge of RV Tauri disks may not be in long-term stable orbits. Artymowicz & Lubow (1996) showed hydrodynamical models for unstable inner-disk rims, so it is possible that material may be stripped by the binary, in particular the companion. This scenario may also explain the X-rays observed in U Mon.

3.6.3 Nature and Origin of X-Ray Emission from U Mon

As a binary system with a CBD, there are a number of processes that can generate the detected X-ray emission. We consider processes from U Mon, the companion, and interactions between the components of the system including the CBD.

If the X-ray emission originates from U Mon, the X-ray luminosity corresponds to an $L_{\rm X}/L_{\rm bol} = 10^{-7}$. Generally, such a ratio is consistent with the X-ray emission that arises from shocks caused by variable winds in O and B stars; however, the X-ray emission from U Mon does not quite follow

the general trend with L_{bol} seen for B stars in the Carina Nebula, which would predict an X-ray luminosity up to an order of magnitude higher (e.g. Nazé et al., 2011). The plasma temperature (> 10 MK) is consistent with hot components found in the Carina O and B stars; however, no fast outflows have been measured from U Mon. Indeed, the large radius of U Mon suggests an escape velocity < 100 km s^{-1}, whereas the plasma temperature requires velocities > 800 km s^{-1} for a strong shock. Such velocities have not been measured from U Mon and are unlikely to be produced by any pulsation-induced shocks in the atmosphere of U Mon (Fokin, 1994), unlike that suggested for X-ray emission from the Cepheid star δ Cep (Engle et al., 2017). Gillet et al. (1990) measured shock amplitudes from spectroscopy for the RV Tauri variables R Sct and AC Her that did not exceed ~ 40 km s^{-1}.

We note that Moschou et al. (2020) recently investigated a mechanism to produce phase-dependent shocked gas X-ray emission in the pulsating atmosphere of classical Cepheids. This mechanism requires the presence of solar-like coronal plasma into which the phase-dependent shocks are driven (Moschou et al., 2020). The detected X-ray emission from U Mon is hotter than that studied by Moschou et al. (2020), and we lack adequate phase coverage to establish the presence of such shocks from U Mon, as well as the necessary signal-to-noise ratio in our XMM X-ray light curve to establish the presence of such shocks from U Mon. A solar-like coronal plasma is an intriguing notion given the detection of a magnetic field (very likely dynamo generated) at the surface of this cool post-AGB star, but there is, so far, no information on any related activity such as flares, stellar spots, or dynamo variability that would be linked to X-ray emission. Furthermore, the ability to sustain a hot stellar corona on such a large evolved star is unclear (Sahai et al., 2015).

Accretion, from a compact disk or infalling material from the large CBD (as discussed in Section 3.6.2), might create shocks that can heat material up to X-ray-emitting temperatures. However, given the stellar properties of U Mon in Table 3.1, it is unlikely that infalling material will reach sufficiently high velocities (< 100 km s^{-1} at the surface of U Mon). If the companion star has a radius ≤ 2 R$_\odot$, which would make the companion consistent with an A-type main-sequence star, infalling material, from the CBD or donated by U Mon via wind Roche lobe overflow (Mohamed

& Podsiadlowski, 2007), can reach speeds in excess of 800 km s^{-1}. Such infalling material can either slam into the surface of the star along magnetic fields or form into an accretion disk around the companion.

An accretion disk forming around the companion could then generate outflows as seen in other post-AGB systems (Gorlova et al., 2012, 2015); however, such outflows have yet to be observed from the U Mon system. If such an outflow exists, its velocity could be sufficient to generate shocks capable of explaining the detected X-ray emission. Detailed monitoring of the Hα emission from U Mon, like that performed of similar systems by Gorlova et al. (2012, 2013), could help establish the presence of accretion-disk-driven outflows.

If the binary companion is the source of X-ray emission, in addition to accretion, coronal activity and radiative stellar winds can produce X-ray emission similar to that given in Table 3.4. However, at $\sim 2.2\ M_{\odot}$ (Table 3.1), a main-sequence companion would be consistent with an early-type A star and unable to support magnetic activity to produce coronal X-ray emission (Stelzer et al., 2006). Furthermore, the bolometric luminosity of such a main-sequence companion is 100 times fainter than U Mon, leading to an $L_{\rm X}/L_{\rm bol}$ of 10^{-5} for the companion, which is an unusually high fraction for an A-type star. Such a high fraction of X-ray emission and a high-temperature plasma are comparable to what is seen from Herbig Ae/Be stars, which are intermediate-mass pre-main-sequence stars embedded in dusty disks (Stelzer et al., 2006, 2008). In the case of Herbig stars, the high plasma temperature suggests that radiative winds are not the emission mechanism, and higher-order binary components, namely, unseen rapidly rotating late-type companions to the A star in a Herbig system, have been suggested as a potential origin for their X-ray emission (Stelzer et al., 2006). Since we have not observed the companion and only have a modest constraint on its mass ($2.2^{+1.0}_{-0.75}$ $M_{\odot}$; see Table 3.1), we cannot exclude the remote possibility that the companion is a compact binary. In such a scenario, the detected X-ray emission would be consistent with enhanced coronal activity from rapidly rotating late-type stars in a close binary system.

We have highlighted a number of potential origins for the X-ray emission from the U Mon system, each with strong implications for the nature and evolution of the system. Additional sup-

porting information, such as further constraints on the companion properties and monitoring of the Hα, like that reported in Bollen et al. (2019), and additional observations of the X-ray emission through the phases of the U Mon pulsation and orbit, is essential to better understand the origin and influence of the X-ray emission.

3.7 Conclusions

We have conducted the most comprehensive characterization yet of an RVb system, U Mon, with observations spanning the largest range of wavelengths (X-ray to millimeter) and the longest range of time ($\sim$ 130 yr).

U Mon, one of the brightest RV Tauri variables of its class, is shown here to be a binary system comprising a 2.07 $M_\odot$ post-AGB star that has lost mass relative to a more massive unevolved 2.2 $M_\odot$ A-star companion, and is surrounded by a large CBD. We obtained new orbital parameters within the errors of the values found by Oomen et al. (2018), by fixing the orbital period as the photometric RVb period. The new periastron value, T_0 = 2452203 days, reveals that the apastron times align with RVb minima (Figure 3.1). Additionally, based on our orbital fit, the argument of periastron ($\omega = 95^\circ$) translates to the long axis of the orbit being roughly aligned along our line of sight. This supports the argument that apastron occurs when the post-AGB star is occulted by the near side of the disk at RVb minimum while the A-type star companion is most revealed at the far side of the inner hole in the CBD. Moreover, we found that the binary's semimajor-axis separation is 5.78 au, which at apastron is comparable to the size range of the inner-disk hole radius ($\sim$ 4.5–9.0 au).

U Mon shows several interesting features, some not yet seen in any other post-AGB binary, such as a magnetic field and most recently X-rays. We found a $\sim$ 10 MK plasma model that is consistent with the X-ray spectra and considered origins from U Mon and/or its companion. We suggest that at apastron the companion may be close enough to strip material from the CBD, creating the X-ray emission observed. This interpretation may agree with the complex morphology found in the interferometric dataset for U Mon by Kluska et al. (2019).

The occurrence of the enhanced Hα at RVb minima (e.g. Pollard et al., 2006) also seems to correspond to when the A-type star companion is most revealed at apastron, implying that since the post-AGB star is shadowed by the CBD at this phase, the enhanced Hα must not be coming from the post-AGB star but rather from the environment around the A-type companion, likely an accretion disk (e.g. Bollen et al., 2019). Recent work has shown that the Hα variation is due to a bipolar jet from the circumcompanion accretion disks in other post-AGB binaries. More time series of optical spectra are needed to investigate the Hα variability in U Mon.

We tested whether additional blackbody components with properties of the A-type star companion would influence U Mon's SED but found that such a companion seems to only be detected in Hα (and possibly X-rays), even at RVb minimum, when it is most revealed in its orbit. The X-ray through millimeter emission, however, is consistent with components that include a hot thermal plasma, the stellar photosphere of the post-AGB, and the inner- and extended-disk emission. The scaling of the modified blackbody for the dust emission includes parameters such as opacity and dust grain sizes that we do not explore in this paper. However, U Mon's new SMA observation fluxes are in agreement with the slope of the Rayleigh-Jeans form of the Planck function, between the other 60–3000 μm flux measurements. Such slopes are consistent with the presence of a composition of large dust grains (radius $\gtrsim$ 0.1 mm; de Ruyter et al., 2005). Due to the short SMA observations, we are only able to estimate upper limits on U Mon's disk diameter size $\lesssim$ 550 au (see Table 3.3).

Nevertheless, with the AAVSO+DASCH light curve, which spans more than 130 yr, we find evidence for a 60.4 yr cycle that could be due to some structure in the disk at a separation of $\sim$ 25 au that temporarily allows the post-AGB star to avoid being occulted at apastron/RVb minimum. Accordingly, the 60.4 yr cycle also produces an especially deeper RVb minimum (phase $\sim$ 54 yr in Figure 3.7–two cycles before the "disappearance" of the RVb minima). Presumably this can be a corresponding feature in the disk that causes an exceptionally large occultation of the post-AGB star. More radio observations at longer baselines would constrain the size of the disk, as well as resolve features we see in U Mon's light curve.

Furthermore, the detection of X-rays from the U Mon system has opened up new possibilities; do all RV Tauri variables exhibit X-ray emission? In order to answer this question, X-rays will be an important factor to consider in forthcoming RV Tauri studies to enable constraints on their evolution (e.g., Graber & Montez, 2021).

Most importantly, U Mon now becomes an archetype for the study of binary post-AGB stellar environments that represent an important evolutionary phase, which either sets the stage for sculpting the morphology and evolution of planetary nebulae or which may represent systems that never become planetary nebulae at all, as the disk and stellar companion arrest its development.

Chapter 4

Conclusions and Future Work

4.1 Conclusion

There is now general agreement that the photometric RVb phenomenon observed in some RV Tauri systems is a binary–star phenomenon, linked to periodic disk obscuration of the pulsating primary star at certain phases of the orbit. This dissertation work has contributed to the field of RV Tauri star studies by providing insight into how binarity plays a role in these systems. In Chapter 2 we demonstrated this by using ~ 4 years of ultra-precise *Kepler* data for the RVb system, DF Cyg, where we found that a 90% reduction in the mean brightness was the same percent–decrease in pulsation-amplitudes, from the RVb maximum to pulsation-amplitudes in the RVb minimum states. This revealed that the amplitudes of the pulsating star are (relatively) constant through out the entire RVb cycle and the dust, from the optically-thick circumbinary disk, periodically obscures the star at RVb minimum. Kiss & Bódi (2017) further proved the dust obscuration model for well-monitored RVb stars in the Galaxy, using AAVSO data, which spanned their longest temporal baseline. Using interferometric near-IR observations, Kluska et al. (2019) also confirmed that the high disk–scale-height in several RVb systems can cause shadowing of the binary system.

In Chapter 3 we introduced photometric data at a even a longer temporal–baseline, using the combination of DASCH and AAVSO data. The 130-year light curve shows secular changes in the RVb behavior for the U Mon RVb system. We suggest that a feature in the circumbinary disk may be causing these brightness changes at decade–long timescales, suggesting disk–evolution behavior at play. However, disk or binary precession should also be considered for causing for these longer–term changes in brightness. Finally, we introduced the first X-ray detection for any RV Tauri star to date (see Figure 4.1), opening new possibilities for the exploration of binary-disk

interaction, accretion, and pulsation shocks at these high-energy regimes for RV Tauri stars. We briefly discuss future work and ideas in the next section.

4.2 Future Work

4.2.1 Multiwavelength Observations of RV Tauri Systems

The study of RV Tauri stars has focused primarily in the optical to infrared wavelengths. With the advent of modern satellite observatories that peer into the X-ray and ultraviolet (UV) we are in a position to probe for new evidence and establish the role of RV Tauri stars in our understanding of stellar evolution. Executing comprehensive multiwavelength studies of RV Tauri stars would reveal unique aspects of their composition and provide a better understanding to distinguish physical processes.

The origin of the X-ray emission from U Mon is unclear, but it suggests that disk-binary interaction may play a significant role and make-up overall (Vega et al., 2021). To determine if X-ray emission from RV Tauri stars is common, more targeted observations are needed. Exciting work lies ahead as we prepare for two candidates to be observed with XMM–*Newton* in the near future. Graber & Montez (2021) are already leading a serendipitous survey of RV Tauri variables in *Swift*, *Chandra*, and XMM–*Newton* archives. They have found many observations of RV Tauri variables but only one other detection has been found so far, besides the one of U Mon. The majority of the RV Tauri stars observed by these X-ray telescopes were in the Magellanic Clouds or in crowded and heavily-extincted fields towards the Galactic Center, thus the upper limits of the new detection are not very constraining. Nevertheless, potential for future detections still exist for a nearby survey.

The pulsational nature of RV Tauri stars still remains poorly understood, as they show to have more irregular behavior compared to the other classical pulsators. Shock models that are currently used to explain RV Tauri stars need updating (e.g., Fokin, 1994; Fadeyev & Gillet, 2004). The overlooked X-ray and UV emission from RV Tauri stars may reveal distinct processes, such as,

of shocks from stellar pulsation outflows, towards surrounding gas. Furthermore, high–energy observations would help to understand how binarity may affect pulsation behavior in general. UV and X-ray emission may also yield results for a stellar continuum of the inner core hidden within the expanding layers (Montez, 2010) or dynamo-generated magnetic fields of the star's convective zone due to deferential rotation (Güdel & Nazé, 2009). It is also important to check for white dwarfs being hot companions. (Chu et al., 2004) suggested that white dwarfs that exhibit hard X-rays may reveal to be binary systems due to this hard X-ray emission in accretion discs from a possibly late-type companion star. If any UV and X-ray emission is not consistent for accretion, shocks, white dwarf companions or coronal activity from a late-type main sequence companion, we can then test against these processes.

There are still many optical light curves which have not been classified in the Kepler/K2 fields, thus, there is room for improvement in pulsation analyses with non-linear hydrodynamic methods, such as those suggested by Plachy et al. (2018), to confirm chaotic dynamics in RV Tauri stars. Kepler/K2 light curves are available in the KSwAgs database (Smith et al., 2015), providing intriguing light curves, that may include unidentified RV Tauri stars or post-AGB binary candidates, and that may have unanalyzed *Swift* X-ray and UV data associated with them. Observations from *Kepler*'s successor, the Transiting Exoplanet Survey Satellite[1] (TESS), can also reveal more promising information to help establish physical processes. TESS' ultra-high precision photometry can further probe pulsational behavior and shocks, which can fundamentally refine our understanding of these stars. This can be done especially by hunting for RV Tauri stars in the regions of the sky known as TESS' continuous viewing zones, where observing segments overlap at the ecliptic poles, providing observation period of 351 days of coverage per year–optimal for observing these long-period stars.

Multiwavelength monitoring RV Tauri system at all phases of their orbits would also provide useful to find correlations across the electromagnetic spectrum. Collaborations such as Gorlova et al. (2012); Oomen et al. (2018); Bollen et al. (2019) have already been monitoring the radial

[1] http://tess.mit.edu/

velocities of post-AGB and RV Tauri variables since 2009 and have been able to obtain tomography of jets produced from an accretion disk around the secondary star in these systems.

4.2.2 Circumbinary Disks

Disk structure, formation, and tracers of disk-evolution around RV Tauri stars is also lacking. With more historic DASCH data becoming available and with the combination of regular monitoring, it will be interesting to learn how the RVb phenomenon changes for other RV Tauri systems at century-long timescales and help understand their disk behavior.

In combination with updated parallax measurements from *Gaia*'s DR3 for distance estimates, time-resolved and higher spatial inerferometric observations are also need. Flux measurements at longer radio wavelengths will constrain their SEDs for dust chemistry models and resolved continuum images will provide direct disk properties, such as inclination, inner-edge, and outer disk diameters. Such radio images can further resolve disk structures to compare with timeseries photometric data.

4.2.3 Accretion Disks

One of the topics of most interest, currently being investigated in the field of post-AGB binaries, is learning about their binary-disk interaction, which has shown to be causing accretion and jets. Accretion disk physics around RV Tauri and other post-AGB binaries is still not well understood; however, there are opportunities to apply techniques from studies of other systems and different mass-scales (Pringle, 1981). The study of accretion disks is an over-arching science area in a lot of multiwavelength astrophysics such disks around black holes (e.g., Schlegel et al., 2016), galactic nuclei (e.g., Smith et al., 2018), X-ray binaries (e.g., Torpin, 2019), solar–system formation (e.g., Pollack et al., 1996), and cataclysmic variables (e.g. Schlegel et al., 1984; Pagnotta et al., 2015). Warped or twisted accretion disks are also invoked to explain phenomena observed across many types of systems from proto-planetary disks (e.g., Wahhaj et al., 2003; Kraus et al., 2020) to active galactic nuclei (Ogilvie & Dubus, 2001). X-ray binaries attribute a lot of their variability

to disks, whether they are tilted or warped (Boyd & Smale, 2004), or to precession of the accretion disks (Still & Boyd, 2004). Similarly, for supermassive black holes in active galaxies, like NGC 4258 (e.g. Bregman & Alexander, 2009), warping mechanism require initial asymmetry in the disk or disk–source alignment for a warp to develop. Methods like recurrence analysis which is the study of recurrent, non-periodic information in non-linear dynamics, and are well-established in other non-astrophysical fields (e.g., geology, economics), were used by Phillipson et al. (2020) to confirm the detection and period of optical quasi-periodic oscillations in AGN accretion disks. These approaches can also be used to fine evidence for physical mechanisms underlying multi-year optical light curves of RV Tauri, in well-sampled TESS data or future data from the upcoming Vera C. Rubin Observatory[2], which will image thousands of objects every night, averaging an estimated 20 TB per night.

Post-AGB stars in binary configurations are one of the most likely explanations for the shaping of nonspherical planetary nebulae, a long-standing question in stellar evolution. However finding correlations across the electromagnetic spectrum, with multiwavelength studies of RV Tauri stars, would then represent a major advance in our understanding of late-stage stellar evolution and the environments in which they form. Consequently, the crossroads in understanding the link between old supergiant stars, binarity, and planetary nebulae may then be complete.

[2] http://www.lsst.org/scientists/keynumbers

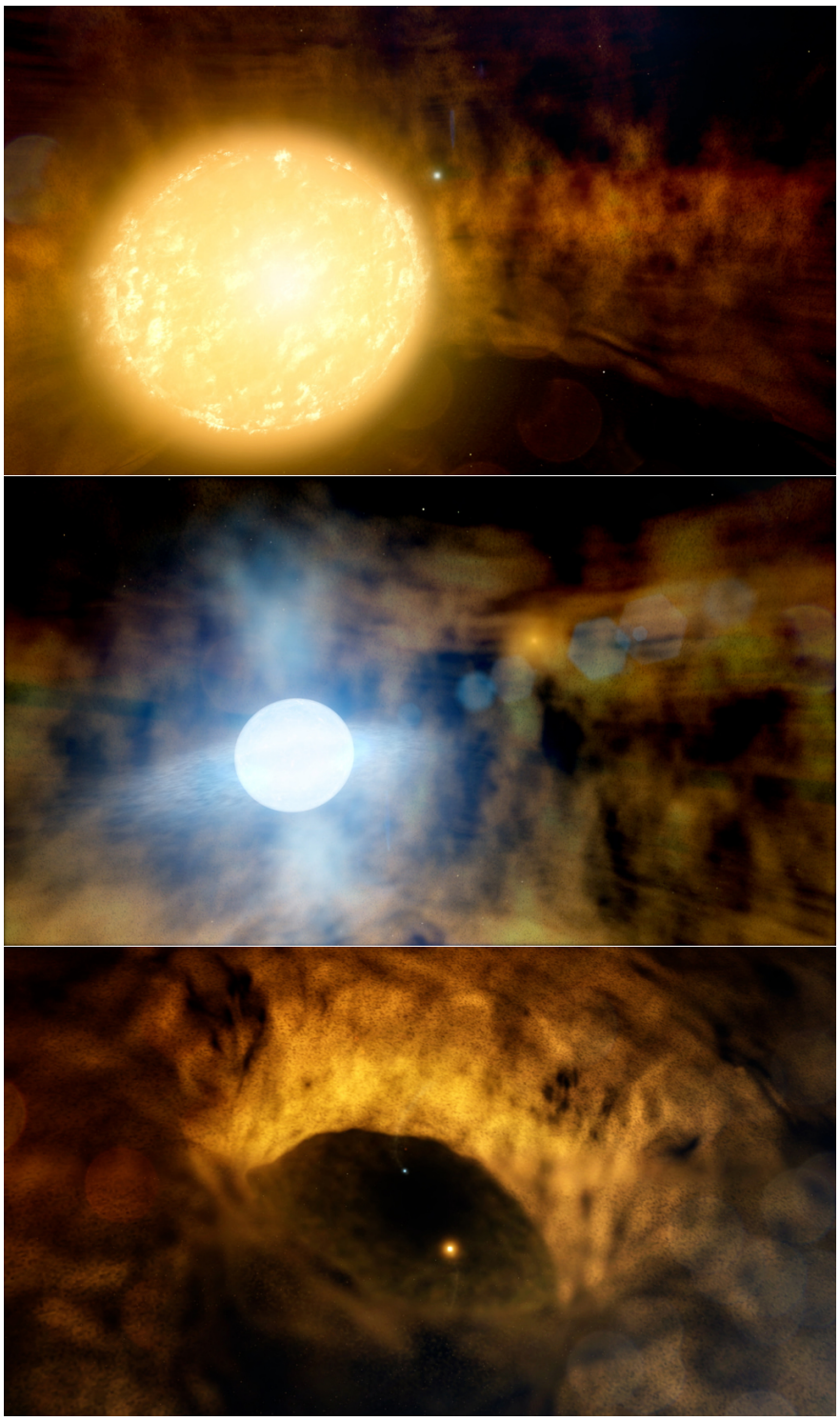

Figure 4.1: Illustrations of the possible configuration of the U Mon RVb system. Top: U Mon's primary RV Tauri star, an elderly pulsating supergiant; the stellar companion and circumbinary disk are seen in the background. Middle: U Mon's secondary star accreting material from the circumbinary disk into its own disk, which heats up and generates an X-ray-emitting outflow. Bottom: Top view of the U Mon binary system inside a circumbinary disk. Credit: NASA's Goddard Space Flight Center/Chris Smith (USRA/GESTAR). NASA new story multimedia for Vega et al. (2021): https://svs.gsfc.nasa.gov/13806

BIBLIOGRAPHY

Alcock, C., Allsman, R. A., Alves, D. R., et al. 1998, AJ, 115, 1921, doi: 10.1086/300317

Anders, E., & Grevesse, N. 1989, GeCoA, 53, 197, doi: 10.1016/0016-7037(89)90286-X

Arnaud, K. A. 1996, XSPEC: The First Ten Years, Vol. 101 (Astronomical Society of the Pacific Conference Series), 17

Artymowicz, P., & Lubow, S. H. 1996, ApJ, 467, L77, doi: 10.1086/310200

Astropy Collaboration, Robitaille, T. P., Tollerud, E. J., et al. 2013, A&A, 558, A33, doi: 10.1051/0004-6361/201322068

Balick, B., & Frank, A. 2002, ARA&A, 40, 439, doi: 10.1146/annurev.astro.40.060401.093849

Basri, G., Johns-Krull, C. M., & Mathieu, R. D. 1997, AJ, 114, 781, doi: 10.1086/118510

Belokurov, V., Penoyre, Z., Oh, S., et al. 2020, MNRAS, 496, 1922, doi: 10.1093/mnras/staa1522

Bladh, S., Höfner, S., Nowotny, W., Aringer, B., & Eriksson, K. 2013, A&A, 553, A20, doi: 10.1051/0004-6361/201220590

Bódi, A., & Kiss, L. L. 2019, ApJ, 872, 60, doi: 10.3847/1538-4357/aafc24

Bódi, A., Szatmáry, K., & Kiss, L. L. 2016, A&A, 596, A24, doi: 10.1051/0004-6361/201629318

Bollen, D., Kamath, D., De Marco, O., Van Winckel, H., & Wardle, M. 2020, A&A, 641, A175, doi: 10.1051/0004-6361/202038414

Bollen, D., Kamath, D., Van Winckel, H., & De Marco, O. 2019, A&A, 631, A53, doi: 10.1051/0004-6361/201936073

Bollen, D., Van Winckel, H., & Kamath, D. 2017, A&A, 607, A60, doi: 10.1051/0004-6361/201731493

Bono, G., Castellani, V., & Marconi, M. 2000, ApJ, 529, 293, doi: 10.1086/308263

Boyd, P. T., & Smale, A. P. 2004, ApJ, 612, 1006, doi: 10.1086/421078

Bregman, M., & Alexander, T. 2009, The Astrophysical Journal, 700, L192, doi: 10.1088/0004-637x/700/2/l192

Brown, T. M., Latham, D. W., Everett, M. E., & Esquerdo, G. A. 2011, AJ, 142, 112, doi: 10.1088/0004-6256/142/4/112

Bujarrabal, V., Alcolea, J., Van Winckel, H., Santander-García, M., & Castro-Carrizo, A. 2013, A&A, 557, A104, doi: 10.1051/0004-6361/201322015

Bujarrabal, V., Castro-Carrizo, A., Alcolea, J., & Neri, R. 2005, A&A, 441, 1031, doi: 10.1051/0004-6361:20053118

Bujarrabal, V., Castro-Carrizo, A., Van Winckel, H., et al. 2018, A&A, 614, A58, doi: 10.1051/0004-6361/201732422

Cardelli, J. A., Clayton, G. C., & Mathis, J. S. 1989, ApJ, 345, 245, doi: 10.1086/167900

Casey, C. M. 2012, MNRAS, 425, 3094, doi: 10.1111/j.1365-2966.2012.21455.x

Catelan, M., & Smith, H. A. 2015, Pulsating Stars (Wiley-VCH)

Ceraski, W. 1905, Astronomische Nachrichten, 168, 29, doi: 10.1002/asna.19051680207

Chu, Y.-H., Guerrero, M. A., Gruendl, R. A., & Webbink, R. F. 2004, AJ, 127, 477, doi: 10.1086/380230

Cox, J. P. 1974, Reports on Progress in Physics, 37, 563, doi: 10.1088/0034-4885/37/5/001

De Marco, O. 2009, PASP, 121, 316, doi: 10.1086/597765

de Ruyter, S., Van Winckel, H., Dominik, C., Waters, L. B. F. M., & Dejonghe, H. 2005, A&A, 435, 161, doi: 10.1051/0004-6361:20041989

de Ruyter, S., Van Winckel, H., Maas, T., et al. 2006, A&A, 448, 641, doi: 10.1051/0004-6361:20054062

Deroo, P., Van Winckel, H., Min, M., et al. 2006, A&A, 450, 181, doi: 10.1051/0004-6361:20054300

Dullemond, C. P., Dominik, C., & Natta, A. 2001, The Astrophysical Journal, 560, 957, doi: 10.1086/323057

Engle, S. G., Guinan, E. F., Harper, G. M., et al. 2017, ApJ, 838, 67, doi: 10.3847/1538-4357/aa6159

Evans, T. L. 1985, MNRAS, 217, 493, doi: 10.1093/mnras/217.3.493

Fadeyev, Y. A., & Gillet, D. 2004, A&A, 420, 423, doi: 10.1051/0004-6361:20040992

Fitzpatrick, E. L., Massa, D., Gordon, K. D., Bohlin, R., & Clayton, G. C. 2019, ApJ, 886, 108, doi: 10.3847/1538-4357/ab4c3a

Fokin, A. B. 1994, A&A, 292, 133

Foster, A. R., Ji, L., Smith, R. K., & Brickhouse, N. S. 2012, ApJ, 756, 128, doi: 10.1088/0004-637X/756/2/128

Gaia Collaboration, Brown, A. G. A., Vallenari, A., et al. 2016a, A&A, 595, A2, doi: 10.1051/0004-6361/201629512

Gaia Collaboration, Prusti, T., de Bruijne, J. H. J., et al. 2016b, A&A, 595, A1, doi: 10.1051/0004-6361/201629272

Gaia Collaboration, Brown, A. G. A., Vallenari, A., et al. 2018, A&A, 616, A1, doi: 10.1051/0004-6361/201833051

Gandhi, P., Buckley, D. A. H., Charles, P., et al. 2020, arXiv e-prints, arXiv:2009.07277. https://arxiv.org/abs/2009.07277

Gehrz, R. D. 1972, ApJ, 178, 715, doi: 10.1086/151829

Gerasimovič, B. P. 1929, Harvard College Observatory Circular, 341, 1

Gezer, I., Van Winckel, H., Bozkurt, Z., et al. 2015, MNRAS, 453, 133, doi: 10.1093/mnras/stv1627

Gielen, C., Van Winckel, H., Matsuura, M., et al. 2009a, A&A, 503, 843, doi: 10.1051/0004-6361/200912060

Gielen, C., Van Winckel, H., Reyniers, M., et al. 2009b, A&A, 508, 1391, doi: 10.1051/0004-6361/200912982

Gielen, C., Bouwman, J., Van Winckel, H., et al. 2011, A&A, 533, A99, doi: 10.1051/0004-6361/201117364

Gillet, D., Burki, G., & Duquennoy, A. 1990, A&A, 237, 159

Giridhar, S., Lambert, D. L., & Gonzalez, G. 2000, ApJ, 531, 521, doi: 10.1086/308451

Giridhar, S., Lambert, D. L., Reddy, B. E., Gonzalez, G., & Yong, D. 2005, ApJ, 627, 432, doi: 10.1086/430265

Gorlova, N., Van Winckel, H., Vos, J., et al. 2013, in EAS Publications Series, Vol. 64, Setting a New Standard in the Analysis of Binary Stars, ed. K. Pavlovski, A. Tkachenko, & G. Torres, 163

Gorlova, N., Van Winckel, H., Vos, J., et al. 2014, ArXiv e-prints. https://arxiv.org/abs/1403.2287

Gorlova, N., Van Winckel, H., Gielen, C., et al. 2012, A&A, 542, A27, doi: 10.1051/0004-6361/201118727

Gorlova, N., Van Winckel, H., Ikonnikova, N. P., et al. 2015, MNRAS, 451, 2462, doi: 10.1093/mnras/stv1111

Graber, S., & Montez, R. 2021, in American Astronomical Society Meeting Abstracts, Vol. 53, American Astronomical Society Meeting Abstracts, 528.05

Green, G. M., Schlafly, E. F., Finkbeiner, D. P., et al. 2015, ApJ, 810, 25, doi: 10.1088/0004-637X/810/1/25

Grindlay, J., Tang, S., Simcoe, R., et al. 2009, in Astronomical Society of the Pacific Conference Series, Vol. 410, Preserving Astronomy's Photographic Legacy: Current State and the Future of North American Astronomical Plates, ed. W. Osborn & L. Robbins, 101

Groenewegen, M. A. T., & Jurkovic, M. I. 2017, A&A, 604, A29, doi: 10.1051/0004-6361/201730946

Groenewegen, M. A. T., Sloan, G. C., Soszyński, I., & Petersen, E. A. 2009, A&A, 506, 1277, doi: 10.1051/0004-6361/200912678

Groenewegen, M. A. T., Wood, P. R., Sloan, G. C., et al. 2007, MNRAS, 376, 313, doi: 10.1111/j.1365-2966.2007.11428.x

Güdel, M., & Nazé, Y. 2009, A&A Rev., 17, 309, doi: 10.1007/s00159-009-0022-4

Hardy, A., Schreiber, M. R., Parsons, S. G., et al. 2016, MNRAS, 459, 4518, doi: 10.1093/mnras/stw976

Hartig, E., Cash, J., Hinkle, K. H., et al. 2014, AJ, 148, 123, doi: 10.1088/0004-6256/148/6/123

Harwood, M. 1927, Harvard College Observatory Bulletin, 847, 5

Harwood, M., & Shapley, H. 1937, Annals of Harvard College Observatory, 105, 521

He, J. H., Szczerba, R., Hasegawa, T. I., & Schmidt, M. R. 2014, ApJS, 210, 26, doi: 10.1088/0067-0049/210/2/26

Hildebrand, R. H. 1983, QJRAS, 24, 267

Hillen, M., de Vries, B. L., Menu, J., et al. 2015, A&A, 578, A40, doi: 10.1051/0004-6361/201425372

Hillen, M., Menu, J., Van Winckel, H., et al. 2014, A&A, 568, A12, doi: 10.1051/0004-6361/201423749

Hillen, M., Van Winckel, H., Menu, J., et al. 2017, A&A, 599, A41, doi: 10.1051/0004-6361/201629161

Höfner, S., & Olofsson, H. 2018, A&A Rev., 26, 1, doi: 10.1007/s00159-017-0106-5

Holman, M. J., & Wiegert, P. A. 1999, AJ, 117, 621, doi: 10.1086/300695

Homan, W., Danilovich, T., Decin, L., et al. 2018, A&A, 614, A113, doi: 10.1051/0004-6361/201732246

Joy, A. H. 1952, ApJ, 115, 25, doi: 10.1086/145506

Jura, M. 1986, ApJ, 309, 732, doi: 10.1086/164642

Kama, M., Min, M., & Dominik, C. 2009, Astronomy and Astrophysics, 506, 1199, doi: 10.1051/0004-6361/200912068

Kamath, D. 2015, in EAS Publications Series, Vol. 71-72, EAS Publications Series, 129–134

Kamath, D., Wood, P. R., Van Winckel, H., & Nie, J. D. 2016, A&A, 586, L5, doi: 10.1051/0004-6361/201526892

Kiss, L. L., & Bódi, A. 2017, A&A, 608, A99, doi: 10.1051/0004-6361/201731876

Kluska, J., Hillen, M., Van Winckel, H., et al. 2018, A&A, 616, A153, doi: 10.1051/0004-6361/201832983

Kluska, J., Van Winckel, H., Hillen, M., et al. 2019, A&A, 631, A108, doi: 10.1051/0004-6361/201935785

Kraus, S., Kreplin, A., Young, A. K., et al. 2020, Science, 369, 1233, doi: 10.1126/science.aba4633

Ladjal, D., Justtanont, K., Groenewegen, M. A. T., et al. 2010, A&A, 513, A53, doi: 10.1051/0004-6361/200913147

Lazareff, B., Berger, J. P., Kluska, J., et al. 2017, A&A, 599, A85, doi: 10.1051/0004-6361/201629305

Lindegren, L., Lammers, U., Hobbs, D., et al. 2012, A&A, 538, A78, doi: 10.1051/0004-6361/201117905

Maas, T., Van Winckel, H., & Waelkens, C. 2002, A&A, 386, 504, doi: 10.1051/0004-6361:20020209

Manick, R., Van Winckel, H., Kamath, D., Hillen, M., & Escorza, A. 2017, A&A, 597, A129, doi: 10.1051/0004-6361/201629125

Manick, R., Van Winckel, H., Kamath, D., Sekaran, S., & Kolenberg, K. 2018, A&A, 618, A21, doi: 10.1051/0004-6361/201833130

Manick, R., Kamath, Devika, Van Winckel, Hans, et al. 2019, A&A, 628, A40, doi: 10.1051/0004-6361/201834956

Marconi, M., Coppola, G., Bono, G., et al. 2015, ApJ, 808, 50, doi: 10.1088/0004-637X/808/1/50

Mason, K. O., Breeveld, A., Much, R., et al. 2001, A&A, 365, L36, doi: 10.1051/0004-6361:20000044

McMullin, J. P., Waters, B., Schiebel, D., Young, W., & Golap, K. 2007, CASA Architecture and Applications, Vol. 376 (Astronomical Society of the Pacific Conference Series), 127

Mohamed, S., & Podsiadlowski, P. 2007, in Astronomical Society of the Pacific Conference Series, Vol. 372, 15th European Workshop on White Dwarfs, ed. R. Napiwotzki & M. R. Burleigh, 397

Monnier, J. D., & Millan-Gabet, R. 2002, ApJ, 579, 694, doi: 10.1086/342917

Monnier, J. D., Millan-Gabet, R., Billmeier, R., et al. 2005, ApJ, 624, 832, doi: 10.1086/429266

Montez, R., J., Kastner, J. H., Balick, B., et al. 2015, ApJ, 800, 8, doi: 10.1088/0004-637X/800/1/8

Montez, Rodolfo, J. 2010, PhD thesis, Rochester Institute of Technology

Moschou, S.-P., Vlahakis, N., Drake, J. J., et al. 2020, ApJ, 900, 157, doi: 10.3847/1538-4357/aba8fa

Nazé, Y., Broos, P. S., Oskinova, L., et al. 2011, ApJS, 194, 7, doi: 10.1088/0067-0049/194/1/7

Ochsenbein, F., Bauer, P., & Marcout, J. 2000, A&AS, 143, 23, doi: 10.1051/aas:2000169

Ogilvie, G. I., & Dubus, G. 2001, MNRAS, 320, 485, doi: 10.1046/j.1365-8711.2001.04011.x

Oomen, G.-M., Pols, O., Van Winckel, H., & Nelemans, G. 2020, A&A, 642, A234, doi: 10.1051/0004-6361/202038341

Oomen, G.-M., Van Winckel, H., Pols, O., & Nelemans, G. 2019, A&A, 629, A49, doi: 10.1051/0004-6361/201935853

Oomen, G.-M., Van Winckel, H., Pols, O., et al. 2018, A&A, 620, A85, doi: 10.1051/0004-6361/201833816

Pagnotta, A., Schaefer, B. E., Clem, J. L., et al. 2015, ApJ, 811, 32, doi: 10.1088/0004-637X/811/1/32

Percy, J. R. 1993, in Astronomical Society of the Pacific Conference Series, Vol. 45, Luminous High-Latitude Stars, ed. D. D. Sasselov, 295

Percy, J. R., Sasselov, D. D., Alfred, A., & Scott, G. 1991, ApJ, 375, 691, doi: 10.1086/170233

Phillipson, R. A., Boyd, P. T., Smale, A. P., & Vogeley, M. S. 2020, MNRAS, 497, 3418, doi: 10.1093/mnras/staa2069

Plachy, E., Bódi, A., & Kolláth, Z. 2018, MNRAS, 481, 2986, doi: 10.1093/mnras/sty2511

Plachy, E., Molnár, L., Kolláth, Z., Benkő, J. M., & Kolenberg, K. 2014, in IAU Symposium, Vol. 301, Precision Asteroseismology, ed. J. A. Guzik, W. J. Chaplin, G. Handler, & A. Pigulski, 473–474

Pollack, J. B., Hubickyj, O., Bodenheimer, P., et al. 1996, Icarus, 124, 62, doi: 10.1006/icar.1996.0190

Pollard, K. H., & Cottrell, P. L. 1995, in Astronomical Society of the Pacific Conference Series, Vol. 83, IAU Colloq. 155: Astrophysical Applications of Stellar Pulsation, ed. R. S. Stobie & P. A. Whitelock, 409

Pollard, K. R., Cottrell, P. L., Kilmartin, P. M., & Gilmore, A. C. 1996, MNRAS, 279, 949, doi: 10.1093/mnras/279.3.949

Pollard, K. R., McSaveney, J. A., & Cottrelll, P. L. 2006, MmSAI, 77, 527

Primiani, R. A., Young, K. H., Young, A., et al. 2016, Journal of Astronomical Instrumentation, 5, 1641006, doi: 10.1142/S2251171716410063

Pringle, J. E. 1981, ARA&A, 19, 137, doi: 10.1146/annurev.aa.19.090181.001033

Prša, A., Conroy, K. E., Horvat, M., et al. 2016, ApJS, 227, 29, doi: 10.3847/1538-4365/227/2/29

Raskin, G., van Winckel, H., Hensberge, H., et al. 2011, A&A, 526, A69, doi: 10.1051/0004-6361/201015435

Rodriguez, J. E., Pepper, J., Stassun, K. G., et al. 2013, AJ, 146, 112, doi: 10.1088/0004-6256/146/5/112

Sabin, L., Wade, G. A., & Lèbre, A. 2015, MNRAS, 446, 1988, doi: 10.1093/mnras/stu2227

Sahai, R., Claussen, M. J., Schnee, S., Morris, M. R., & Sánchez Contreras, C. 2011, ApJ, 739, L3, doi: 10.1088/2041-8205/739/1/L3

Sahai, R., Sanz-Forcada, J., Sánchez Contreras, C., & Stute, M. 2015, ApJ, 810, 77, doi: 10.1088/0004-637X/810/1/77

Samus, N. N., Durlevich, O. V., & et al. 2009, yCat, 1, 2025

Schlegel, E. M., Jones, C., Machacek, M., & Vega, L. D. 2016, ApJ, 823, 75, doi: 10.3847/0004-637X/823/2/75

Schlegel, E. M., Kaitchuck, R. H., & Honeycutt, R. K. 1984, ApJ, 280, 235, doi: 10.1086/161990

Skrutskie, M. F., Cutri, R. M., Stiening, R., et al. 2006, AJ, 131, 1163, doi: 10.1086/498708

Smith, K. L., Mushotzky, R. F., Boyd, P. T., et al. 2018, ApJ, 857, 141, doi: 10.3847/1538-4357/aab88d

Smith, K. L., Boyd, P. T., Mushotzky, R. F., et al. 2015, AJ, 150, 126, doi: 10.1088/0004-6256/150/4/126

Smith, R. K., Brickhouse, N. S., Liedahl, D. A., & Raymond, J. C. 2001, ApJ, 556, L91, doi: 10.1086/322992

Soszyński, I., Udalski, A., Szymański, M. K., et al. 2017, Acta Astron., 67, 297, doi: 10.32023/0001-5237/67.4.1

—. 2020, Acta Astron., 70, 101, doi: 10.32023/0001-5237/70.2.2

Stelzer, B., Micela, G., Hamaguchi, K., & Schmitt, J. H. M. M. 2006, A&A, 457, 223235, doi: 10.1051/0004-6361:20065006

Stelzer, B., Robrade, J., Schmitt, J. H. M. M., & Bouvier, J. 2008, A&A, 493, 11091119, doi: 10.1051/0004-6361:200810540

Still, M., & Boyd, P. 2004, ApJ, 606, L135, doi: 10.1086/421349

Tang, S., Grindlay, J., Los, E., & Servillat, M. 2013, PASP, 125, 857, doi: 10.1086/671760

Thompson, S. E., Everett, M., Mullally, F., et al. 2012, ApJ, 753, 86, doi: 10.1088/0004-637X/753/1/86

Torpin, T. J. 2019, PhD thesis, The Catholic University of America

Tsesevich, V. P. 1975, Pulsating Stars (New York: Wiley), 112

van Winckel, H. 2003, ARA&A, 41, 391, doi: 10.1146/annurev.astro.41.071601.170018

van Winckel, H. 2017, in Planetary Nebulae: Multi-wavelength Probes of Stellar and Galactic Evolution, ed. X. Liu, L. Stanghellini, & A. Karakas, Vol. 323, 231–234

—. 2018, arXiv e-prints. https://arxiv.org/abs/1809.00871

van Winckel, H., Waelkens, C., Fernie, J. D., & Waters, L. B. F. M. 1999, A&A, 343, 202

van Winckel, H., Waelkens, C., Waters, L. B. F. M., et al. 1998, A&A, 336, L17

van Winckel, H., Lloyd Evans, T., Briquet, M., et al. 2009, A&A, 505, 1221, doi: 10.1051/0004-6361/200912332

Vega, L. D., Stassun, K. G., Montez, Jr., R., Boyd, P. T., & Somers, G. 2017, ApJ, 839, 48, doi: 10.3847/1538-4357/aa67dd

Vega, L. D., Stassun, K. G., Montez, R., et al. 2021, The Astrophysical Journal, 909, 138, doi: 10.3847/1538-4357/abe302

Venn, K. A., Puzia, T. H., Divell, M., et al. 2014, ApJ, 791, 98, doi: 10.1088/0004-637X/791/2/98

Wahhaj, Z., Koerner, D. W., Ressler, M. E., et al. 2003, ApJ, 584, L27, doi: 10.1086/346123

Wallerstein, G. 2002, PASP, 114, 689, doi: 10.1086/341698

Waters, L. B. F. M., Trams, N. R., & Waelkens, C. 1992, A&A, 262, L37

Watson, C. L., Henden, A. A., & Price, A. 2006, Society for Astronomical Sciences Annual Symposium, 25, 47

Weidemann, V. 1990, ARA&A, 28, 103, doi: 10.1146/annurev.aa.28.090190.000535

Willson, L. A., & Templeton, M. 2009, in American Institute of Physics Conference Series, Vol. 1170, American Institute of Physics Conference Series, ed. J. A. Guzik & P. A. Bradley, 113–121

Wilms, J., Allen, A., & McCray, R. 2000, ApJ, 542, 914, doi: 10.1086/317016